

Transitions in the strain hardening behaviour of tempered martensite

L.Y. Wang^{1,2,*}, Y.X. Wu², W.W. Sun³, Y. Bréchet², L. Brassart⁴, A. Arlazarov⁵, C.R. Hutchinson²

¹ State Key Laboratory of Rolling and Automation, Northeastern University, Shenyang, 110819, China

² Department of Materials Science and Engineering, Monash University, Clayton, VIC 3800, Australia

³ School of Materials Science and Engineering, Southeast University, Nanjing, 211189, China

⁴ Department of Engineering Science, University of Oxford, Oxford OX1 3PJ, United Kingdom

⁵ ArcelorMittal Global Research and Development, Voie Romaine-BP30320, 57283, Maizières-les-Metz,
France

*Corresponding Author: wanglingyu@ral.neu.edu.cn

Keywords: Tempered martensite, advanced high strength steels (AHSS), strain hardening, composite model, kinematic hardening, alloying element effect, Bauschinger effect.

Abstract

Martensite is a key constituent in advanced high strength steels (AHSS). The mechanical response of martensite has received particular attention in recent years due to its very high strain hardening rate. Previous studies have shown that the strain hardening behaviour of as-quenched and low temperature tempered martensite can be described by considering martensite as a composite, with constituents showing a spectrum of yield strengths or residual transformation stresses, or more likely, a combination of both effects. However, the composite models are unable to explain the flow behaviour of martensite tempered above 400 °C when the composite effect starts to diminish and a transition in the strain hardening behaviour is observed. In this contribution, we conduct a systematic study on the flow behaviour of high temperature tempered martensite with three AHSS compositions. The evolution of the strain hardening behaviour is studied using monotonic and tension-compression tests while the evolution in microstructures is monitored using thermal analysis, interrupted X-ray diffraction and microscopy. A continuous loss of strain hardening capacity is observed in all steels during tempering at lower temperatures due to the diminishing composite effects. When the tempering temperature is above 500 °C, all samples show strain hardening rates below the E/50 limit for dislocation storage and a gradual increase in the strain hardening capacity is observed during tempering. To rationalise the tension-compression flow behaviour of martensite tempered at 600 °C, a combined isotropic and kinematic hardening model considering dislocation storage and back stresses generated at cementite particles is proposed. The need to combine the composite models that work well for as-quenched and low temperature tempered martensite, with the dislocation-based models that work well for high temperature tempered martensite, is discussed in the context of self-consistently describing the transitions in strain hardening behaviour as a function of tempering temperature.

1 Introduction

Martensite plays a critical role in many steels. It is an important component of the advanced high strength steels (AHSS) used in the automotive industry, and due to its versatility in strength and ductility after quenching and tempering, it is also the fundamental constituent in virtually all high strength steels [1]. The mechanical response of martensite has received particular attention in recent years due to its very high strain hardening rate [2–8]. Models have been developed that interpret the mechanical response in terms of a composite effect due to the sequential nature of the martensite transformation during cooling. Some models assume a spectrum of local yield strengths in the microstructure [2–4], others a spectrum of residual transformation stresses [5–7], and more recently, an “integral composite model” that combines both effects [8]. The latter model by Wang et al. [8] has demonstrated that the high strain hardening rate in as-quenched and low temperature (300 °C and 400 °C) tempered martensite can be successfully described by considering the convolution of a yield strength spectrum and a residual stress spectrum. However, deviations from the model are observed as the tempering temperature increases. For example, samples tempered at 400 °C for 1 hour show a significant decrease in the strain hardening rate as a result of diminishing composite strengthening effects. This change in the strain hardening response motivates us to investigate the transition in the flow behaviour from martensite tempered at low temperatures, where the composite effects dominate, to martensite tempered at higher temperatures where the composite effects are less obvious.

The major findings on the mechanical properties of high temperature tempered martensite have been summarised by Speich and Leslie before the 1970s [9,10]. Since then, Krauss and collaborators have systematically studied the mechanical properties of tempered martensite especially in AISI 41xx and 43xx steels [11–16]. A summary of their works can be found in several recent review articles by Krauss [17–19]. These studies mainly focused on the evolution of the yield strength (YS) and ultimate tensile strength (UTS). For these strength related parameters, the depletion of solute carbon and reduction in the transformation induced dislocation density lead to reductions in both YS and UTS after tempering. The decrease in strength is accelerated at higher temperatures (typically above 600 °C - 700 °C) when cementite coarsening and recrystallisation becomes dominant [14]. The stress-strain curves of martensite tempered above 400 °C starts to become flat and show limited strain hardening compared to the as-quenched and low temperature tempered conditions [19]. As a result, the strain hardening rate of high temperature tempered martensite drops immediately after yield and remains low until the point of necking. This comparatively weak strain hardening response is very different to its low temperature tempered counterpart where the strain hardening rate is always above the E/50 limit for dislocation storage based strengthening [8,20].

Modelling the strength and strain hardening behaviour of high temperature tempered martensite is usually based on the evolution of the dislocations and their interactions with obstacles in martensite. Galindo-Nava and Rivera-Díaz-del-Castillo interpreted the martensite recovery process as a result of carbon diffusing away from dislocation arrays at lath boundaries which allowed the authors to estimate the evolution of the dislocation density using the diffusion kinetics of carbon [21]. Together with the estimation of block size (grain size strengthening) and precipitation kinetics (precipitate strengthening), the authors were able to describe the yield

strength of tempered martensite. However, early work by Malik and Lund suggested that the grain size strengthening contribution is not very important and the yield strength may be described using only the dislocation density and the mean inter-particle spacing of cementite [22]. In terms of the strain hardening behaviour, Cupertino Malheiros et al. used a simplified continuous composite model to describe the flow behaviour of tempered martensite tempered up to 500 °C [23]. Their model shows that yield stress spectrum width decreased during tempering and this was correlated with the carbon content in the matrix. While this simplified composite model can reproduce the flow curve of tempered martensite, X-ray diffraction results (shown later) indicate that the composite effect is reduced at tempering temperatures above 400 °C and the composite model may have difficulties in treating elevated tempering conditions [8]. Kim et al. took a different approach [24], and developed a combined isotropic and kinematic hardening model to address the monotonic plasticity of a series of Si containing medium carbon steels. The isotropic hardening was due to dislocation storage and the kinematic hardening was attributed to the pile-up of dislocations at high angle grain boundaries. Although the modelling results were promising, some of the physical parameters were not clearly quantified and the contribution from kinematic hardening was not verified by dedicated experiments, such as Bauschinger experiments. On the other hand, secondary particles such as cementite will also provide a kinematic hardening contribution [25–28]. Early work by Chang and Asaro did include Bauschinger test results of a spheroidised high carbon steel, and these authors proposed that the kinematic hardening contribution comes primarily from the formation of Orowan loops on cementite particles [29]. The existence of substructure boundaries does not contribute to the build-up of kinematic hardening but tends to reduce the magnitude of the back stress as they may provide relaxation sites for Orowan loops if cementite particles are located on the substructure boundaries. These contradicting views on the kinematic hardening and the overall strain hardening of high temperature tempered martensite require additional experimental and theoretical works to resolve these important outstanding questions. Although there are studies devoted to the modelling of the low cycle fatigue behaviour of tempered martensitic steels [30,31], systematic modelling of the large-strain tension-compression behaviours of high temperature tempered martensite is lacking.

A further important aspect in tempered martensite is the effect of alloying elements. Si and Al are both added to 3rd generation AHSS to promote carbon partitioning and austenite stabilisation by delaying cementite precipitation. While their effects on cementite precipitation and solute partitioning have been extensively investigated in the literature [32–34], their effect on martensite softening is usually studied using hardness tests, and does not reflect the change in strain hardening behaviour [32,35,36]. The relative potency of Si and Al in resisting martensite softening is also debatable. Zhu et al. suggested that Si is more effective at lower tempering temperatures (i.e. ≤ 400 °C) but Al is more effective at high tempering temperature and longer tempering times [35]. However, Bauschinger test results from Wang et al. showed that kinematic hardening accounts for a large proportion of the flow stress in tempered martensite and Si is more effective than Al in resisting the reduction in kinematic hardening for all tempering conditions between 300 °C and 600 °C [37].

In this contribution, a systematic study of the flow behaviour of tempered martensite with Si and Al additions by monotonic tensile tests is conducted. The evolution of martensite softening is linked to the microstructural

evolution and chemistry effects using thermal analyses, microstructural characterisations, and X-ray diffraction. Interrupted X-ray diffraction experiments [8] are extended to high temperature tempering regimes and demonstrate a clear transition in the strain hardening behaviour of tempered martensite. This transition is influenced by the addition of Si and Al. A gradual increase in the strain hardening capacity is also observed during further tempering at 500 °C and 600 °C regardless of alloying additions. Based on the quantification of Orowan loops on cementite precipitates, a combined isotropic and kinematic hardening model is developed to explain both the monotonic tension and tension-compression flow behaviour of martensite tempered at 600 °C. The limitations of the current treatments to martensite strain hardening, as well as the future work required to develop a unified description of the plastic response of martensite as a function of tempering conditions is discussed.

2 Experimental procedure

The materials used in this study were provided by ArcelorMittal and their compositions from chemical analysis are shown in Table 1. The base composition is Fe-0.25C-2.5Mn (wt.%). Si and Al were added to study the effect of alloying elements on martensite softening. The steels were supplied as both cold rolled (CR) sheets (~1.2 mm thick) and hot rolled (HR) plates (~6 mm thick). The CR sheets were used for monotonic tensile tests and microstructural characterisations under various tempering conditions. The HR plates were used to perform tension-compression Bauschinger tests for selected conditions. The austenitization experiments were conducted in a horizontal tube furnace heated to 950 °C with flowing Ar for 10 minutes followed by water quenching. The tempering experiments were performed in a salt bath (300 °C- 600 °C) for various times followed by water quenched after tempering.

Table 1 The chemical compositions of the investigated steels (wt.%)

Designation (reference composition)		Fe	C	Mn	Si	Al	P	S
Base steel (Fe-0.25C-2.5Mn)	CR	Bal.	0.24	2.4	<0.02	0.01	0.01	0.01
	HR	Bal.	0.25	2.43	<0.02	0.01	0.01	0.01
Si steel (Fe-0.25C-2.5Mn-1.4Si)	CR	Bal.	0.25	2.42	1.44	0.01	0.01	0.01
	HR	Bal.	0.24	2.4	1.45	0.01	0.01	0.01
Al steel (Fe-0.25C-2.5Mn-1.4Al)	CR	Bal.	0.27	2.46	0.02	1.38	0.01	0.01
	HR	Bal.	0.26	2.52	0.02	1.42	0.01	0.01

Monotonic tensile tests were conducted on an Instron 4505 screw-driven machine with a 100 kN load capacity and using a clip-on 10 mm extensometer. The crosshead speed was fixed at 0.02 mm/s (equivalent strain-rate $\sim 1.67 \times 10^{-3} \text{ s}^{-1}$). Samples with a gauge length of 12 mm and width of 5 mm were electrodischarge machined from the CR sheets parallel to the rolling direction. All mechanical properties presented in this work were determined using the true stress-true strain curve. While the ultimate tensile strength (UTS) can be directly

determined using the Considère's criterion, the yield strength (YS) was defined using the 0.2% proof stress. The strain hardening exponent n was estimated using the Hollomon equation ($\sigma = K\varepsilon_p^n$, σ is the true stress, K is the strength coefficient and ε_p is the true plastic strain). For samples with continuous yielding, the portion between the YS and UTS was fitted. For tensile curves exhibiting yield discontinuities and yield point elongations (YPE), only the portion after the yield discontinuity was considered. Figure S1 shows examples of $\ln \sigma - \ln \varepsilon_p$ curves for the Si steel tempered at different temperatures for 5 minutes to demonstrate the suitability of the fitting for the hardening exponent, n . The linear regressions can be fitted well to the experimental curves ($R^2 \geq 0.95$). Tension-compression Bauschinger tests were performed to quantify the evolution of the back stress and kinematic hardening. Some of the Bauschinger test results have been published in a separate contribution [37] and part of the experimental tension-compression curves for high temperature tempered samples are reproduced here to inform the proposed plasticity model. Samples tempered at 600 °C for 24 hours were also tested to demonstrate the validity of the proposed plasticity model in heavily tempered martensite.

X-ray diffraction (XRD) was used to investigate the peak profile of tempered martensite before and after deformation. Samples were cut from either the undeformed head or the deformed gauge section of the CR tensile samples and polished to 0.05 μm surface finish with colloidal silica. The XRD experiments were conducted on a Bruker D8 Advance diffractometer with a Co tube (operated at 40 kV and 25 mA) under the Bragg-Brentano geometry. X-ray scans were performed over the $38^\circ \sim 132^\circ$ 2θ range at a step size of 0.03° to capture the (110), (200), (211) and (220) diffraction peaks. XRD analysis was performed in the Bruker-TOPAS (version 5) software and the strain broadening is phenomenologically described using Balzar's double-Voigt approach [38]. All four peaks were used in the calculation of the microstrain. It should be noted that the peak broadening has contributions from both transformation induced residual stresses and dislocations, and proper line profile analysis such as the convolutional multiple whole profile (CMWP) method [39–41] may be pursued when both contributions can be modelled simultaneously.

Differential scanning calorimetry (DSC) was used to study the effect of Si and Al additions on the cementite precipitation kinetics. Samples were taken from the undeformed grip section and sectioned to $\sim 4 \text{ mm} \times 4 \text{ mm} \times 0.1 \text{ mm}$ dimensions, which corresponds to a typical sample weight of $\sim 100 - 120 \text{ mg}$. DSC was performed using a Perkin Elmer Pyris 1 with a heating rate of $25^\circ\text{C}/\text{min}$ between 20°C to 500°C . Before the tests, calibration of the equipment was performed using In and Zn standards.

Scanning electron microscopy (SEM) was conducted with a JEOL JSM-7001F field emission gun (FEG) SEM using secondary electron imaging (SEI) with a 10 kV accelerating voltage to reveal cementite precipitates. All samples examined by SEM were cut from the undeformed head section and polished to $1 \mu\text{m}$ surface finish and etched with either 4% Picral for cementite precipitates or 2% Nital for additional grain boundary contrast. Electron backscattered diffraction (EBSD) was used to reveal the evolution of martensite substructures. The accelerating voltage in EBSD mode was 15 kV, the probe current was 18 nA, and a Nordlys-II EBSD detector and the Oxford Instruments AZtec software suite were used. The scan area on each sample is $60 \mu\text{m} \times 60 \mu\text{m}$

and the scanning step size is 0.1 μm . The indexing rates were above 85% for all samples with a 0.05 μm surface finish and most non-indexed points were found at high angle grain boundaries. Post-processing of EBSD data was conducted using the TSL-OIM 8 software. One iteration of neighbour misorientation correlation was conducted to clean the data. Grains were defined by a 15° misorientation and a minimum area of 3 pixels. The size of a grain was defined as its equivalent circular diameter (ECD) and the average grain size is calculated as the arithmetic average of all grain diameters. The above definition gives an estimation of the average block size, similar to the approach of Kim et al. [24].

Transmission electron microscopy (TEM) was performed to quantify the number of Orowan loops stored on cementite precipitates. To allow accurate correlation with Bauschinger test results, all TEM specimens were prepared from the HR plate. Monotonic tests were interrupted at different total strains and slices of $\sim 350\ \mu\text{m}$ in thickness were cut from the deformed gauge of the sample. The slices were mechanically ground to $\sim 100\ \mu\text{m}$ before 3 mm diameter discs were punched from the slices. The discs were electropolished with the Struers Tenupol-5 twin-jet polishing system in a 3.5 vol. % perchloric acid in methanol at a temperature of $-25\ ^\circ\text{C}$ and a voltage of 50 V. The samples were examined on an FEI Tecnai G² T20 TEM operated at 200 kV.

3 Results

3.1 Microstructural evolution in tempered martensite

3.1.1 Evolution of precipitates

The addition of Si and Al to the base steel composition affects predominantly the cementite precipitation kinetics in martensite during tempering. DSC results in Figure 1 demonstrate the effect of alloying elements in the present study. Three distinct exothermic events can be found in all steels with different peak temperatures. The first peak corresponds to the precipitation of transition carbides whose position is chemistry independent. Positions of the second and third peaks in the Si and Al steels match closely the results of De Moor et al. on steels with similar compositions [42]. The second peak corresponds to the decomposition of retained austenite (less than 1% in the as-quenched state as determined by XRD), and the third peak represents the precipitation of cementite. It is clear that the addition of Si and Al postpones the onset of cementite precipitation to higher temperatures ($\sim 400\ ^\circ\text{C}$ cf. $300\ ^\circ\text{C}$ in the Base steel). High magnification SEM imaging was used to confirm the alloying element effect on precipitation. For the Base steel, a high density of plate shaped carbides can be found after tempering at $300\ ^\circ\text{C}$ (Figure 2a). In the case of the Si steel and the Al steel, tempering at $300\ ^\circ\text{C}$ results in much more sparsely spaced, thin plate-shaped carbides (Figure 2b and c). Since the DSC results show that the onset of austenite decomposition and cementite are postponed to $\sim 400\ ^\circ\text{C}$ in the Si steel and the Al steel, the carbides found here should be a mixture of transition carbides and cementite, similar to previous observations [32,34]. As the tempering temperatures rise to $600\ ^\circ\text{C}$, spheroidisation of cementite can be observed in all steels regardless of the presence of alloying elements (Figure 2d – f). While the addition of Si and Al retards the growth of cementite and promotes Mn partitioning [34], the overall tempering response at high temperatures seems unchanged.

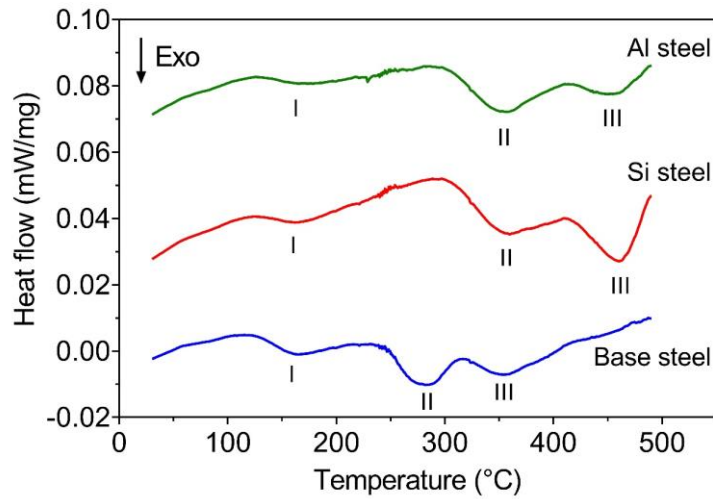


Figure 1 DSC heat flow results for the Base steel, the Si steel and the Al steel heated at a heating rate at 25 °C/min, the three major exothermic peaks were represented by Roman letters.

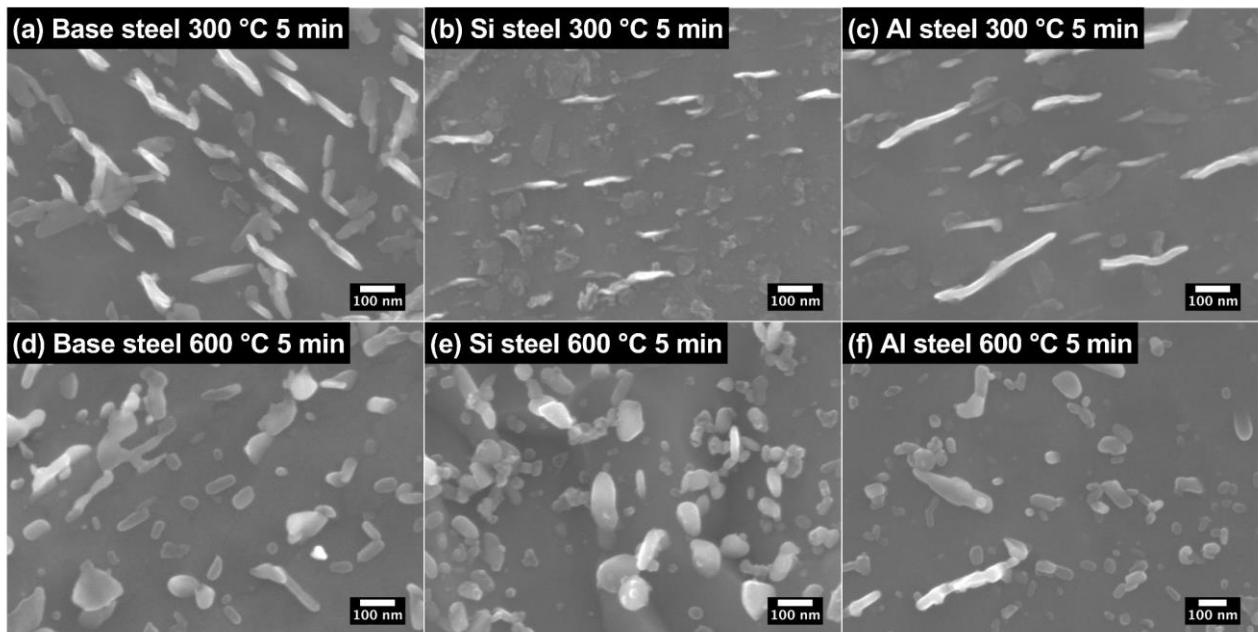


Figure 2 SEM images of precipitates found in the Base steel, the Si steel and the Al steel tempered at 300 °C (a) – (c) and 600 °C (d) – (f).

3.1.2 Evolution of microstrain

The evolution of microstrain, as measured by X-ray diffraction, is used to monitor the recovery kinetics in martensite (Figure 3a, b and c), and may include both residual transformation stress relaxation and dislocation recovery. In the as-quenched state, all steels have a similar level of microstrain which is likely due to the similar carbon content of the steels. During tempering, the decrease in microstrain occurs quickly and is visible after only 1 minute for all tempering temperatures. The magnitude of the initial microstrain drop increases with increasing tempering temperature. For the same tempering temperature, the microstrain also decreases gradually with time but the kinetics of microstrain reduction at longer times is much slower compared to the initial decrease. This fast-to-slow transition in the recovery kinetics is true for all steels regardless of alloy composition. Similar findings can be found in the work of Wu and the slower kinetics occurring at longer

tempering times may be described using conventional dislocation recovery mechanisms [36]. The faster kinetics at shorter times cannot be described by dislocation recovery and is likely related to the relaxation of residual transformation stresses.

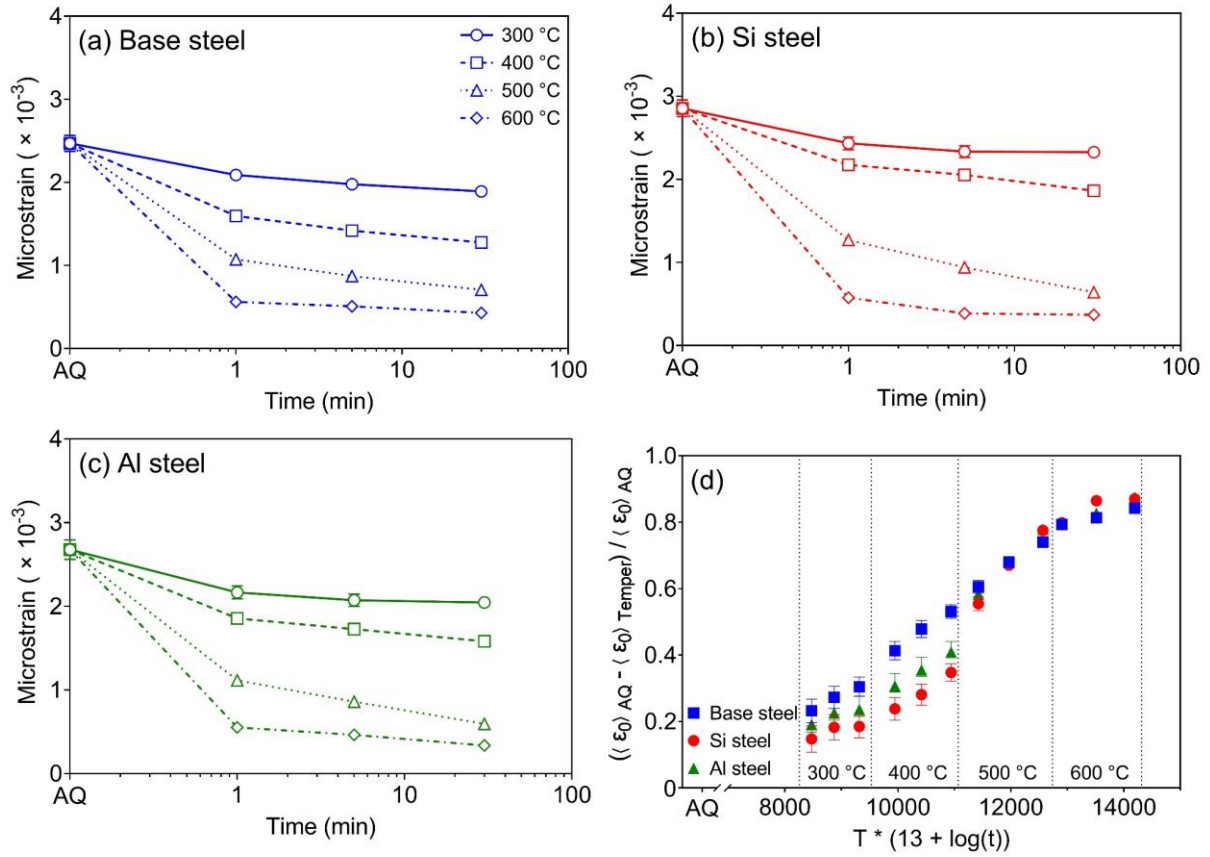


Figure 3 Evolution of the microstrain during tempering of the Base steel (a), the Si steel (b) and the Al steel (c). Error bars represent two times the Rietveld error which include most of uncertainties associated with sample to sample variation. Some error bars are not visible as the bars are smaller than the height of the symbol. (d) Hollomon-Jaffe plot showing the evolution of softening parameters for the microstrain as a function of tempering parameters. At each temperature, three tempering times are shown (i.e. 1 minute, 5 minutes and 30 minutes). Error bars are calculated using the error propagation function.

The addition of Si and Al reduces the magnitude of the initial microstrain drop and slows down the kinetics of its reduction at 300 °C and 400 °C. The relative potency of Si and Al in resisting the drop in microstrain is shown in Figure 3d where the differences between the as-quenched states and the tempered states are normalised by the magnitude of the as-quenched states (i.e. $\frac{\langle \epsilon_0 \rangle_{AQ} - \langle \epsilon_0 \rangle_{Temper}}{\langle \epsilon_0 \rangle_{AQ}}$, denoted as the *softening parameter* in the following text). The “Tempering parameter” $TP = T * (13 + \log t)$, proposed by Hollomon and Jaffe, is shown on the x-axis to enable the comparison between different tempering temperatures and times [23,43]. Si is more effective at resisting microstrain reduction compared to Al. The plot also shows that while the Si and Al affect the recovery kinetics at lower temperatures (300 °C and 400 °C), this effect disappears when the temperature is raised above 500 °C. The chemistry dependence of the microstrain evolution may be interpreted as a consequence of the slower precipitation kinetics in the Si and Al steels: if the cementite precipitation is retarded by the addition of Si and Al at lower temperatures, supersaturated carbon atoms can

segregate to dislocations and reduce their mobility. At higher temperatures, all steels show the same precipitation response which results in similar recovery of the microstrain.

3.2 Evolution of monotonic tension behaviours

3.2.1 Evolution of tensile and strain hardening curves

Figure 4a, c and e show the true stress - true strain curves for the Base, Si and Al steels in both the as-quenched and tempered states. Part of the results have been presented in a previous publication (i.e. the as-quenched, 300 °C and 400 °C tempered samples) [8]. Compared to the as-quenched and low temperature tempered samples, the uniform elongation increases after tempering above 500 °C. Yield discontinuities are seen in the tensile curve for the Base steel and the Si steel tempered above 300 °C (Figure 4c) and for the Al steel tempered above 400 °C (Figure 4e). The discontinuities develop into yield point elongations resembling the Lüders band found in low carbon ferritic steels [44]. The presence of yield discontinuities and YPE upon tempering implies that dislocations are pinned by carbon atmospheres and the degree of pinning increases with increasing temperatures. The details of this change in the yielding behaviour of tempered martensite have not been studied in depth but it is suggested that the decrease in dislocation density during tempering could be the cause of this phenomenon [19,45].

Figure 4b, d and f show the evolution of the strain hardening response. Yield discontinuities and YPEs appear as inflection points on the Kocks-Mecking (K-M) plots and a recovery of strain hardening rates can be found beyond the YPE region, resembling the behaviours of transformation induced plasticity (TRIP) steels. Since the as-quenched microstructures do not have detectable retained austenite, and any retained austenite should be decomposed after high temperature tempering, the recovery of strain hardening capacity can only come from the unpinning of locked dislocations. When the tempering temperature is below 500 °C, the strain hardening rates after the yield discontinuities share a similar slope with the as-quenched condition and a significant portion of the curve is above the E/50 limit, which can be described by the composite models [2,5,8]. For samples tempered above 500 °C, the maximum strain hardening rates after YPEs are always around or below the E/50 limits, which indicates that the classical dislocation storage mechanisms may be more suitable to describe the strain hardening of martensitic steels tempered at high temperatures.

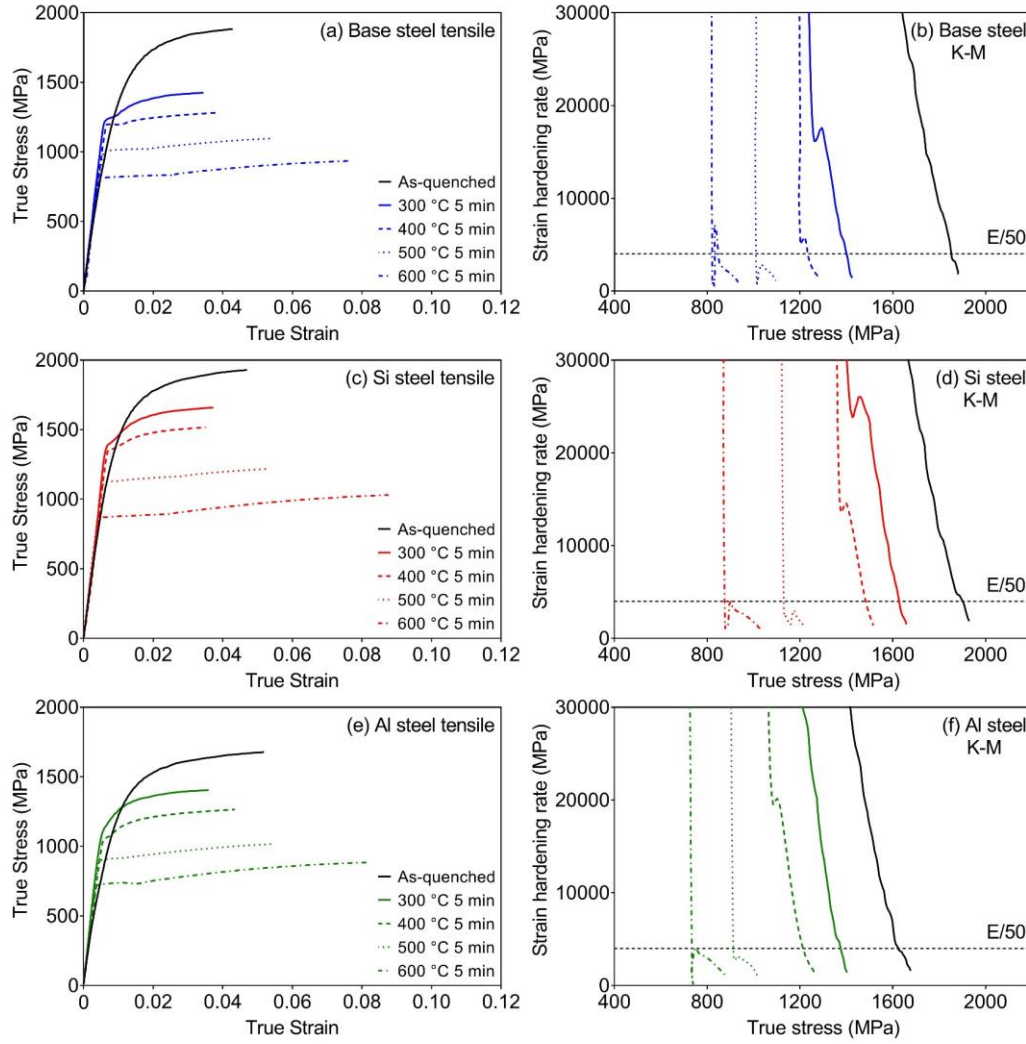


Figure 4 True stress - true strain and strain hardening rate – true stress curves for the Base steel (a and b), the Si steel (c and d) and the Al steel (e and f) with different heat treatment conditions. Results for as-quenched, 300 °C and 400 °C tempered samples have been shown in our previous work [8]. Tensile and Kocks-Mecking plots of all tensile tests conducted on CR samples can be found in Figure S2 of the supplementary materials.

3.2.2 Evolution of mechanical properties and the effect of alloying elements

Figure 5a and b show the evolution of yield strength (0.2% proof strength) and ultimate tensile strength during tempering. The Si steel shows a higher strength than the base steel due to the solid solution strengthening effect of Si. The lower yield strength of the Al steel at all heat treatment conditions is due to its larger prior austenite grain size (~20 μm cf. ~8 μm in the Base and Si steels). Compared to the as-quenched state, the YS of all steels remains relatively constant at 300 °C and 400 °C while the UTS decreases continuously during tempering. This difference in softening kinetics implies that softening of martensite at lower temperatures is primarily attributed to the decrease in the strain hardening response between the YS and UTS. Supporting evidence can be found in Figure 5c where the evolution of the strain hardening exponent is plotted as a function of tempering parameters. The strain hardening exponents of all steels first witnesses a continuous drop to a minimum value ~0.04 when tempered at 300 °C and 400 °C and then gradually increase when tempered above 500 °C for

longer times. The significant decrease in the UTS of martensite tempered at 300 °C and 400 °C is caused by the reduction in strain hardening as a result of the diminishing composite effect [8]. For samples tempered at 500 °C and 600 °C, whilst the strain hardening capacity by dislocation storage mechanisms may be recovered at high temperatures, both YS and UTS decrease significantly.

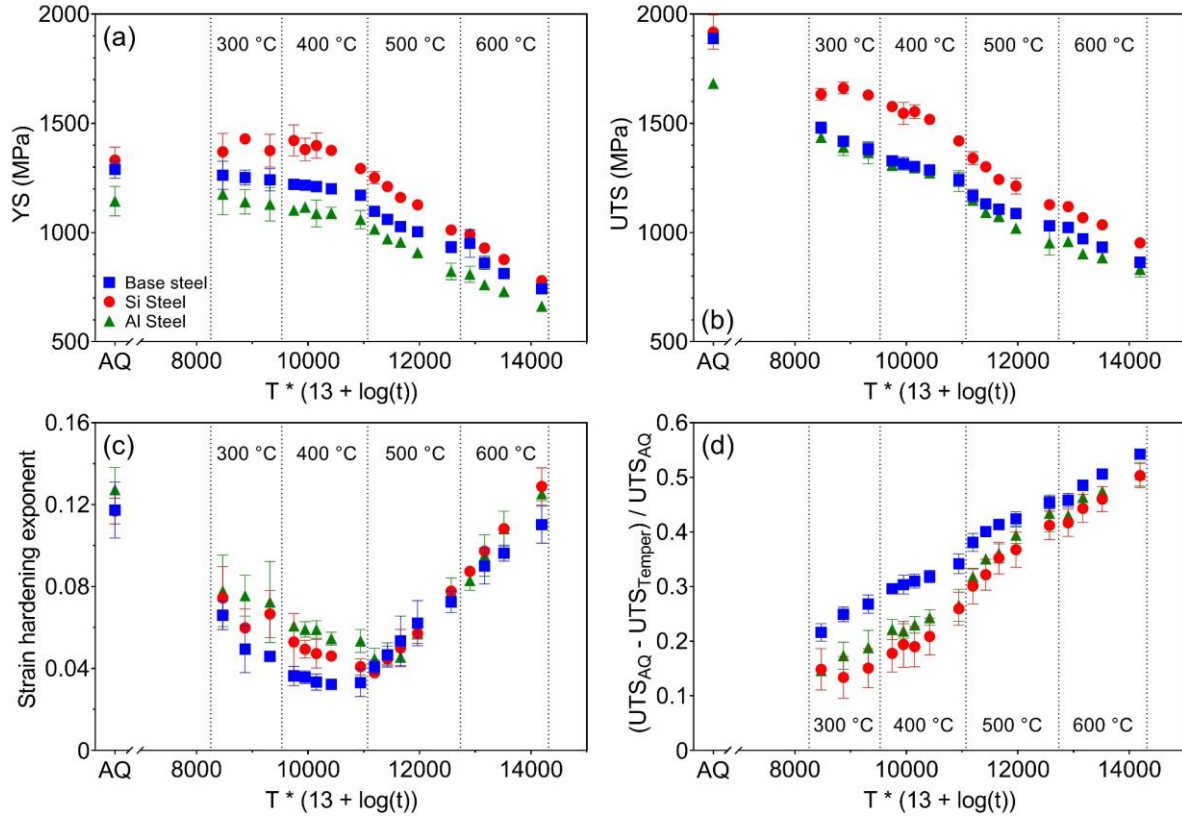


Figure 5 Hollomon-Jaffe plots showing evolution of the YS (a), UTS (b), strain hardening exponents (c) and softening parameters calculated based on the UTS (d) as a function of tempering parameters.

Figure 5c also demonstrates that the addition of Si and Al retards the decrease in the strain hardening exponent at 300 °C and 400 °C. As a consequence, the softening of Si and Al steels at 300 °C and 400 °C is noticeably slower compared to the Base steel as shown in the evolution of the softening parameters of UTS (defined as the difference between the as-quenched states and the tempered states normalised by the magnitude of the as-quenched states, Figure 5d). The larger strain hardening exponent in the Al steel at lower tempering temperatures also explains its comparable UTS to the Base steel although it has a lower YS. On the other hand, the alloying element effect at higher tempering temperatures (i.e. ≥ 500 °C) is less significant as a result of the less chemistry dependent strain hardening exponent. In terms of the relative potency of Si and Al on retarding martensite softening, Si is slightly more effective at lower tempering temperatures (300 °C and 400 °C) but the difference tends to decrease when the temperature is raised above 500 °C. This may be linked to the spheroidisation of cementite occurring during high temperature tempering and its limited chemistry dependency (Figure 2d-f and [33,34]).

3.2.3 Evolution of microstrain during deformation

The high strain hardening rates in as-quenched and low temperature tempered martensite can be characterised by the diffraction peak narrowing phenomenon during deformation [5,6,8]. Interrupted X-ray diffraction experiments have been used to examine the high temperature tempered samples. Figure 6a – c show the effect of tempering and straining on the evolution of microstrain. To the left of the vertical dashed line, the figures show that tempering leads to a decrease in microstrain (as shown in Figure 3). To the right of the dashed line, the figures show the effect of monotonic straining on the microstrain evolution. Compared to the Base steel, the Si and Al steels show less diffraction peak narrowing when tempered at lower temperatures, especially at 400 °C. Together with the results shown in Figure 5, one may conclude that Si and Al slow down the softening of martensite by suppressing the thermal relaxation of transformation induced residual stresses, which has not been previously recognised. When the tempering temperature is above 500 °C, the diffraction peak narrowing phenomenon is replaced by diffraction peak broadening and the composite effect seems to be removed. This is a classic representation of Taylor strengthening which supports the hypothesis made previously that dislocation storage mechanisms are responsible for the strain hardening in high temperature tempered martensite. Therefore, dislocation storage-based models should be considered in order to quantitatively describe the strain hardening of high temperature tempered martensite. The major change in the diffraction peak profile during straining between 400 °C and 500 °C suggests that there exists a transition point at which the transformation induced heterogeneities are quickly removed, leading to the steep reduction in microstrain during short-time tempering at high temperatures.

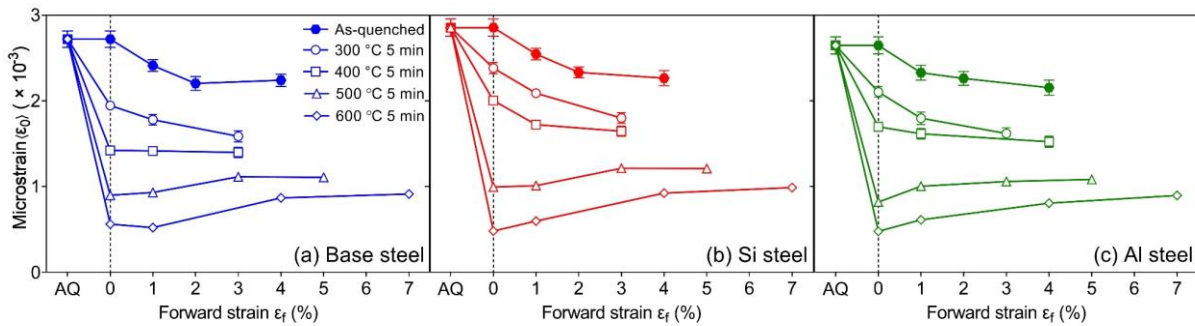


Figure 6 Evolution of microstrain as a function of straining for the Base steel (a), the Si steel (b) and the Al steel (c) tempered at different temperatures for 5 minutes. Error bars in all plots represent two times the Rietveld error. Some error bars are not visible as the bars are smaller than the height of the symbol. Results for as-quenched, 300 °C and 400 °C tempered samples have been shown in our previous work [8].

3.3 Microstructural origin of the back stress at high tempering temperatures

Previous work has shown that both as-quenched and tempered martensite display large kinematic hardening and lead to large Bauschinger effects. The back stress persists even in the high temperature tempered samples (500 °C and 600 °C) but saturates at large forward plastic strains [37]. If the tempering time is prolonged at 600 °C, the saturation level of the back stress also decreases regardless of the alloy composition (Figure 7). For as-quenched and low temperature tempered samples, the large kinematic hardening was attributed to the composite strengthening effect [8]. However, it has been shown in previous sections that the composite effect

diminishes at high tempering temperatures. The development of the back stress in high temperature tempered samples likely comes from the deposition of Orowan loops on secondary precipitates as proposed by Brown and co-workers [25–28]. The back stress saturates at large plastic strains as a result of the number of Orowan loops on each precipitate reaching a maximum. In this section, the microstructural evidence for this hypothesis is shown and a quantitative model describing the kinematic hardening contribution will be implemented later.

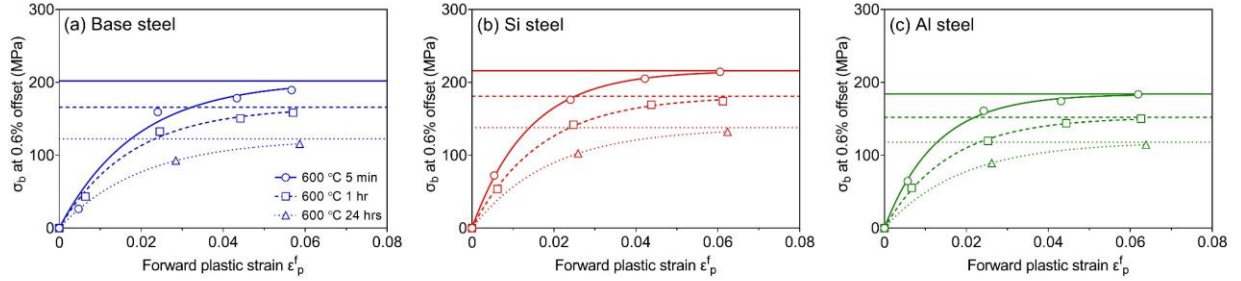


Figure 7 Evolution of 0.6% offset back stresses as a function of forward plastic strain for samples tempered at 600 °C in the case of the Base steel (a), the Si steel (b) and the Al steel (c). The 5-minute and 1-hour results have been previously shown in [37]. The continuous lines are obtained by fitting the experimental back stress data with the phenomenological non-linear kinematic hardening model ($\sigma_b = 2/3 \cdot C/\gamma \cdot \exp(-\gamma\epsilon_p)$, C describes the effective hardening modulus and γ takes into account the dynamic recovery of hardening) [46]. The horizontal lines represent the modelled saturation level as $2/3 \cdot C/\gamma$.

Following the work of Laird and co-workers [47,48] and da Costa Teixeira et al. [49], diffraction-contrast TEM was used to estimate the spacing of Orowan loops on cementite particles instead of measuring the number of Orowan loops directly since the maximum number of loops should scale with the particle radius [49]. Figure 8a is a TEM micrograph of a deformed Base steel sample under two-beam conditions. Cementite particles are highlighted with white arrows and alternating bright and dark contrasts can be observed on the particles. These patterns may be identified as closely packed dislocations since they have ragged edges compared to the sharp interfaces found in the case of Moiré fringes [47,48]. Figure 8b shows an enlarged area of Figure 8a and the spacing between bright and dark contrasts is $\sim 3\text{--}4$ nm. To ensure that the contrast is indeed from deformation-induced Orowan loops, TEM was also performed on tempered samples before straining. It can be seen that the particles do not show the same contrast as the deformed ones (Figure 8c). While some alternating bright and dark contrasts can be found at the edge of the particles (Figure 8d), they only appear at the edges and the interface between the bright and dark regions are much sharper compared to the ones observed in Figure 8b. Therefore, these contrasts may be associated with surface defects or Moiré fringes at the particle-matrix interface. The contrasts found Figure 8a and b should be indeed attributed to the existence of Orowan loops as suggested by Laird and co-workers [47,48]. Nevertheless, rigorous $g \cdot b$ analyses are required to verify the operating Burgers vectors of the dislocation loops [47], which will be investigated in detail in future works.

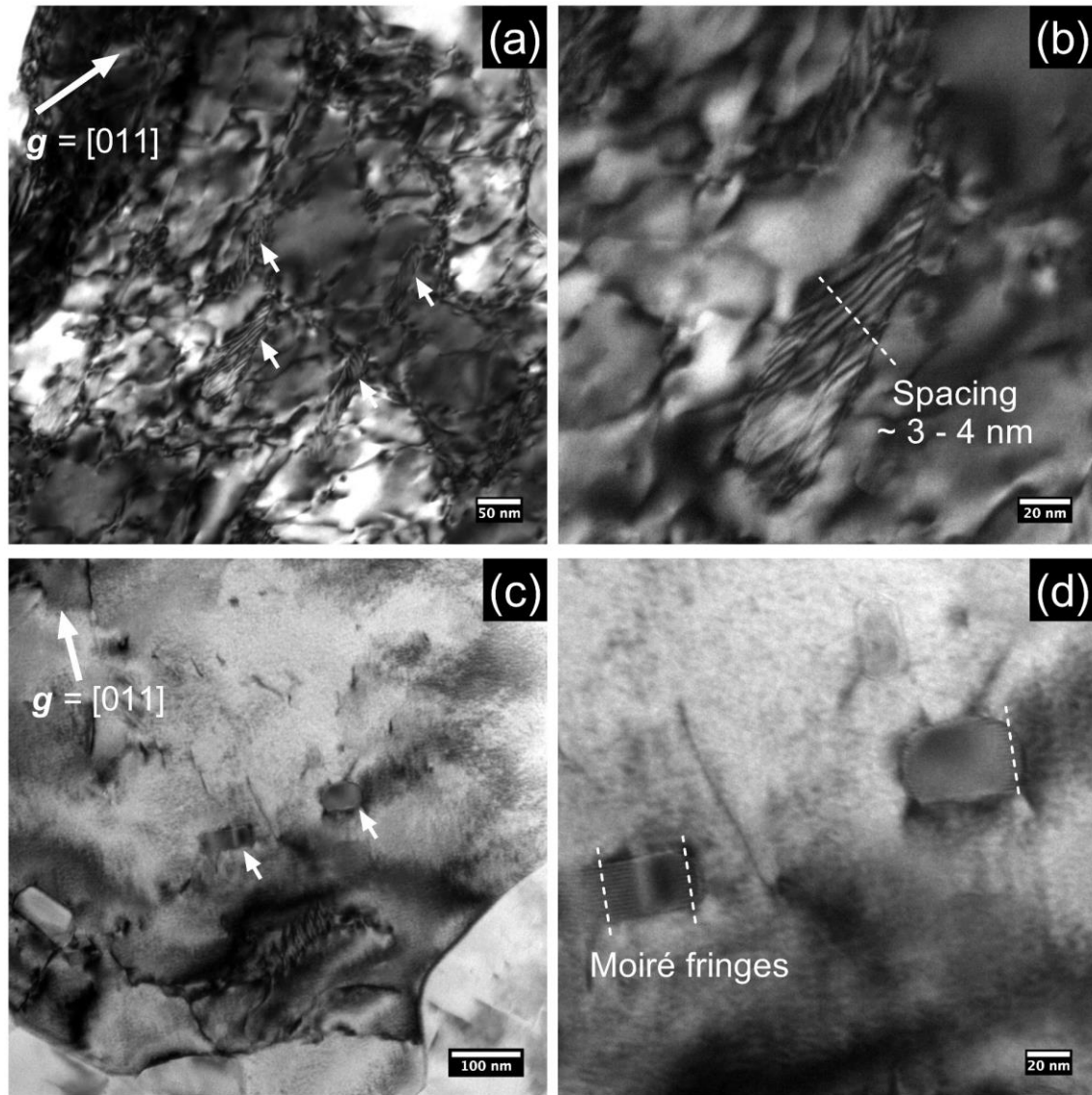


Figure 8 (a) TEM micrograph showing multiple particles with Orowan loops (highlighted by white arrows). The Base sample was deformed to ~7% plastic strain after being tempered at 600 °C for 1 hour. Experimental tensile curves of the HR samples can be found in the supplementary materials Figure S3. The electron beam direction is close to the $[1\bar{2}2]$ zone axis and the operating g vector is shown in the inset. (b) An enlarged area of (a) showing a single particle and spacing between Orowan loops. (c) TEM micrograph showing multiple particles with Moiré fringes (highlighted by white arrows). The Base steel sample was tempered at 600 °C for 1 hour but not deformed. The electron beam direction is close to the $[100]$ zone axis and the operating g vector is shown in the inset. (d) An enlarged area of (c) showing two particles with Moiré fringes at the particle-matrix interface.

The same two-beam TEM characterisation was also performed on the Si and Al steels after deforming to different plastic strains (Figure 9). The loop spacing is relatively constant at plastic strains greater than 2% and not sensitive to the addition of alloying elements. Due to the presence of yield point elongations in high temperature tempered samples, TEM experiments were not performed on samples interrupted inside the Lüders band. However, the loop spacing should decrease at low plastic strains as predicted by the back stress evolution. Similar observations have been made in the Al-Cu system by da Costa Teixeira et al. [49]. The evolution of the loop spacing agrees with the model by Brown and Stobbs [25,26], which suggests that the saturation in the back stress is a result of the saturation of Orowan loops deposited on precipitate particles.

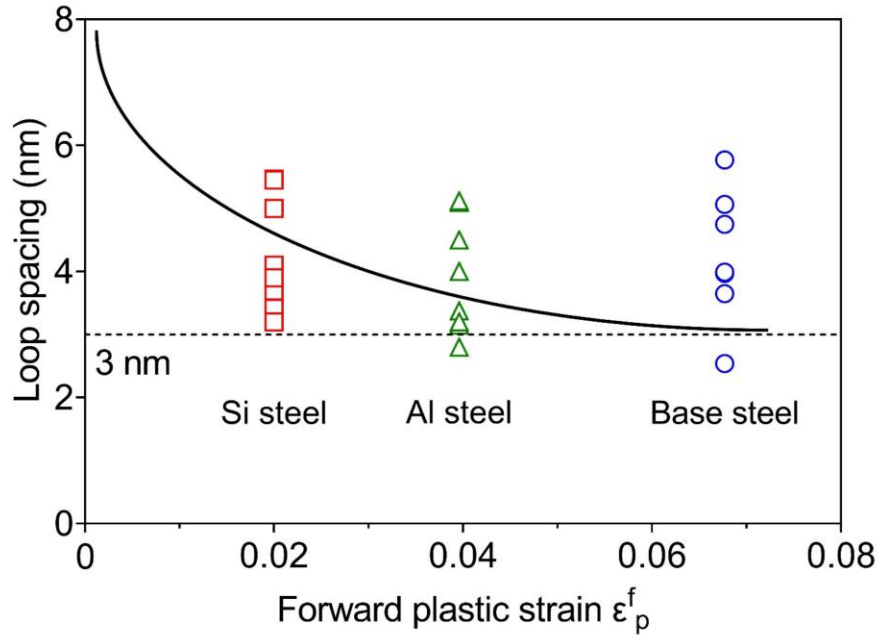


Figure 9 Evolution of the spacing of Orowan loops during plastic deformation. All samples were tempered at 600 °C for 1 hour before deformation. The dashed line represents the minimum loop spacing used in the proposed model and the solid line is added for legibility.

An important consideration with the cementite particles in high temperature tempered martensite is their heterogeneous distribution. Figure 10 shows SEM micrographs of the Si steel after tempering at 600 °C for different times. An increasing number of particles can be found on the martensite lath boundaries instead of inside the laths as the tempering time increases. The precipitates on the boundaries should be less effective in storing dislocation loops compared with the precipitates within the grain due to the large defect density at grain boundaries [29]. This assumption may explain the reduced kinematic hardening contributions for samples tempered at 600 °C for longer times.

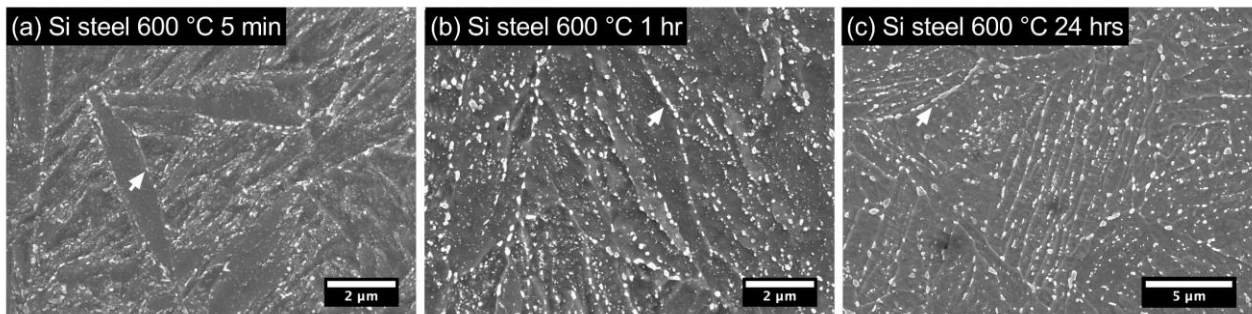


Figure 10 SEM micrographs showing the cementite particles within grains and on grain boundaries. All samples were from the Si steel and were tempered at 600 °C for 5 minutes (a), 1 hour (b) and 24 hours (c). Typical grain boundaries are highlighted with arrows. Etched with Picral.

4 Modelling and discussion

4.1 Modelling the flow behaviour of high temperature tempered martensite

The flow behaviour of as-quenched and tempered martensite can be separated into two regimes depending on the magnitude of the strain hardening rate, which is correlated with tempering temperature. Different modelling approaches are required to rationalise the mechanical response of martensite depending on the tempering conditions. An “integral composite model” has been previously proposed for as-quenched and low temperature tempered martensite where the high strain hardening rate is described by a composite effect induced by the sequential nature of the martensitic transformation [8]. The flow behaviour of high temperature tempered martensite, on the other hand, is more similar to ferrite-cementite steels and the material is predominantly strengthened by dislocation-based mechanisms (Figure 4 and Figure 6). As a result, an attempt is made to model the strain hardening behaviour of high temperature tempered martensite with a combined isotropic and kinematic hardening model in a continuum mechanics framework. While the isotropic hardening comes from dislocation storage, the kinematic hardening is attributed to the presence of cementite precipitates. Although the fine grain size in tempered martensite can also lead to kinematic hardening due to dislocation pile-ups at grain boundaries, quantification of modelling parameters used in such a model require more theoretical and experimental justifications [24,50,51]. Moreover, it is suggested that grain boundaries in ultra-fine grained materials are effective dislocation sinks that do not allow substantial dislocation pile-ups [52].

4.1.1 Kinematic hardening

Kinematic hardening from secondary particles was proposed by Brown and Stobbs [28] and further developed by Proudhon et al. [53] and da Costa Teixeira et al. [49]. If the particles are shear-resistant and able to support dislocation loops, the generated back stress may be described by:

$$\langle \sigma \rangle_{ppt} = M^2 g D \mu V_f \varepsilon_p^{*max} \left[1 - \exp \left(- \frac{\varepsilon_p}{\varepsilon_p^{*max}} \right) \right], \quad \varepsilon_p^{*max} = \frac{n_{ppt}^* b}{2Mr} \quad (1)$$

where M is the Taylor factor, g is the accommodation factor, D is the modulus correction factor, μ is the shear modulus of the matrix, V_f is the volume fraction of secondary particles, ε_p^* is the unrelaxed plastic strain, n_{ppt}^* is the maximum number of loops that can be supported by one particle which is used to calculate the maximum unrelaxed plastic strain ε_p^{*max} , b is the magnitude of the Burgers vector and r is the particle radius. For spherical particles under multi-slip conditions [28], $g = (7 - 5\nu)/20(1 - \nu)$, ν is the Poisson's ratio (estimated as 0.3). The modulus factor can be calculated using the shear moduli of cementite (μ_θ) and ferrite (μ) [28]: $D = \mu_\theta / [\mu_\theta - g(\mu_\theta - \mu)]$. μ_θ is set as 74 GPa according to first principle calculations by Jiang et al. [54] and the experimental work by Laszlo and Nolle [55]. μ is calculated as $\mu = E/2(1 + \nu)$.

For high temperature tempered martensite, it can be assumed that the equilibrium volume fraction of cementite is achieved soon after the tempering starts [33,34]. As a result, the total volume fraction (V_f^{tot}) is set to be 0.0375 (at 600 °C) for all steels since they share similar carbon contents and the addition of Si and Al only affects slightly the equilibrium volume fraction. Therefore, n_{ppt}^* is the only parameter that needs to be quantified in Eq. 1. In the current model, this parameter is estimated using a loop spacing ($2r/n_{ppt}^*$) of 3 nm,

which is around the lower limit of the experimentally measured values (Figure 9). It is also assumed that the loop spacing is independent of the particle radius so that the same spacing is used for all tempering conditions [49], which allows the model to be implemented without prior knowledge of the precipitate size.

In addition, two physical parameters are used to estimate the fraction of cementite precipitates within grains (V_f^g) and the loop spacing for precipitates on the grain boundaries (expressed as $\eta \cdot 2r/n_{ppt}^*$). While the value of V_f^g should decrease as a function of tempering, the factor η is kept constant ($\eta=2.5$) for all tempering conditions since the potency of grain boundary precipitates in storing Orowan loops should not be affected by thermal treatments. This modification to the Brown-Stobbs model also allows the particles with large loop spacing to be considered and reduce the uncertainties in the estimation of n_{ppt}^* .

4.1.2 Isotropic hardening

The classic Kocks-Mecking model and the derived Voce law is used to describe the isotropic contribution to the hardening of the high temperature tempered martensite [20]:

$$\sigma_{iso} = \frac{\theta_0}{\beta_0} [1 - \exp(\beta_0 \varepsilon_p)] \quad (2)$$

where $\theta_0 = \alpha M^2 \mu b k_1 / 2$ and $\beta_0 = k_2 M / 2$. k_1 is a constant that considers the self-trapping efficiency of dislocations and k_2 accounts for the annihilation of dislocations due to dynamic recovery. According to Kocks and Mecking, the maximum θ_0 value can be estimated by $E/50$ [20], resulting in a maximum k_1 value of $\sim 1.5 \times 10^8$ MPa. A varying k_2 would suggest that the annihilation rate of dislocation changes as a function of tempering. This might be due, for example, to the change in the grain boundary spacing during high temperature tempering since grain boundaries are effective sinks for dislocations [56,57].

4.1.3 Elasto-plastic model

The proposed isotropic and kinematic hardening laws are combined in a 3-D elasto-plastic model and applied to simulate uniaxial loading. The initial strain and stress tensors are set to be zero. During straining, the yield function of the material is written as:

$$f = J_2(\boldsymbol{\sigma} - \langle \boldsymbol{\sigma} \rangle_{ppt}) - \sigma_{iso} - \sigma_{y0} \leq 0 \quad (3)$$

where J_2 is the second invariant of the deviatoric stress, $\langle \boldsymbol{\sigma} \rangle_{ppt}$ is the deviatoric tensor that represents the kinematic hardening from cementite precipitates, σ_{iso} and σ_{y0} are the scalars that describe the isotropic hardening and the yield strength. Since precipitates within grains and precipitates on grain boundaries contribute differently to kinematic hardening, $\langle \boldsymbol{\sigma} \rangle_{ppt}$ can be further written as:

$$\langle \boldsymbol{\sigma} \rangle_{ppt} = \langle \boldsymbol{\sigma} \rangle_{ppt}^g + \langle \boldsymbol{\sigma} \rangle_{ppt}^{gb} \quad (4)$$

where $\langle \boldsymbol{\sigma} \rangle_{ppt}^g$ represents precipitates within grains and $\langle \boldsymbol{\sigma} \rangle_{ppt}^{gb}$ represents precipitates on grain boundaries. In each case, the evolution of the back stress can be expressed in the tensor form by combining the Brown-Stobbs model and the Armstrong-Frederick type kinematic hardening law [46,58]:

$$\dot{\langle \boldsymbol{\sigma} \rangle}_{ppt}^g = \frac{2}{3} C^g \dot{\boldsymbol{\varepsilon}}_p - \gamma^g \langle \boldsymbol{\sigma} \rangle_{ppt}^g \dot{p} \quad (5)$$

$$\langle \dot{\sigma} \rangle_{ppt}^{gb} = \frac{2}{3} C^{gb} \dot{\epsilon}_p - \gamma^{gb} \langle \sigma \rangle_{ppt}^{gb} \dot{p} \quad (6)$$

where $\dot{\epsilon}_p$ and \dot{p} are the rates of plastic strain and accumulated plastic strain. $C^g = M^2 g D \mu V_f^g$ and $C^{gb} = M^2 g D \mu (V_f^{tot} - V_f^g)$ are the hardening parameters. $\gamma^g = 2Mr/(n_{ppt}^* b)$ and $\gamma^{gb} = \eta \cdot 2Mr/(n_{ppt}^* b)$ are the recovery parameters in the kinematic hardening model. V_f^{tot} represents the total volume fraction of precipitates. In the current implementation, the magnitudes of $\dot{\epsilon}_p$ and \dot{p} are estimated by the incremental $\Delta \epsilon_p$ and Δp , both of which can be determined by the macroscopic strain increment $\Delta \epsilon$ using appropriate integration schemes.

Due to the presence of yield point elongations in the high temperature tempered samples, the true yield strength of the samples should be smaller than the offset strength measured on the Lüders band [59]. In this case, no effort was made to estimate the yield strength with additive rules [24], rather the interception between $\sigma = E\epsilon$ and $\sigma = K\epsilon^n$ was used since the samples follow the Hollomon hardening law quite well. This intercept is then the strength of the material at zero plastic strain (σ_{y0}), which is the same method used in the work of Chang and Asaro on heavily tempered high-carbon martensite [29]:

$$\sigma_{y0} = \left(\frac{K}{E^n} \right)^{\frac{1}{1-n}} \quad (7)$$

At each time step, a strain increment $\Delta \epsilon$ is applied along the z-direction of the material and the stress increment $\Delta \sigma$ can be calculated using the return-mapping algorithm proposed by Sawyer et al. which considers the combined isotropic and kinematic hardening [60]. Modelling parameters that are set to be constant in all tempering conditions are summarised in Table 2.

Table 2 Fixed parameters used in the combined isotropic and kinematic hardening model.

Parameter	Description	Value	Comment/Reference
E	Young's modulus of ferrite	205 GPa	Measured
ν	Poisson's ratio	0.3	Estimated
μ	Shear modulus of ferrite	79 GPa	Calculated
μ_θ	Shear modulus of θ	74 GPa	[54,55]
g	Accommodation factor	0.39	Calculated
D	Modulus correction factor	0.97	Calculated
M	Taylor factor	2.75	[61]
V_f^{tot}	Total volume fraction of precipitates	0.0375	Calculated, Thermo-Calc
$2r/n_{ppt}^*$	Orowan loop spacing	3 nm	Measured
η	Factor considering grain boundary precipitates	2.5	Estimated
α	Dislocation-dislocation junction strength	0.38	[62]

b	Burgers vector	0.248 nm	
k_1	Coefficient of dislocation self-trapping efficiency	1.5×10^8 MPa	Estimated

4.1.4 Modelling results of 600 °C tempered samples

Figure 11a, c and e show the modelled and experimental results for all steels tempered at 600 °C for 5 minutes, 1 hour and 24 hours. The tension-compression curves are plotted as a function of cumulative strain for clarity. The existence of yield point elongations leads to much lower apparent yield stresses compared to the conventional 0.2% proof stresses, which may lead to uncertainties in the description of the yielding behaviour of the material. However, these estimated yield stress values and the proposed model allows the self-consistent modelling of both monotonic and tension-compression behaviours and show good agreement with experimental results. Globally, the modelled strain reversal behaviour shows worse agreement compared with the monotonic behaviour. The modelled monotonic curves can be found in Figure S3 of the supplementary materials. In all cases, the model demonstrates that the reverse curves can strengthen at the same rate as the forward curves but the experimental results show smaller hardening rates and permanent softening at large reverse strains. This discrepancy is especially obvious in the 24-hour tempered conditions. The inaccuracy of the model at larger reverse strains is attributed to the simplicity of the non-linear hardening law and the lack of permanent softening descriptions in the model. The model can be improved by incorporating permanent softening theories such as the Yoshida-Uemori model in continuum mechanics [63,64] and the Rauch-Gracio-Barlat-Vincze (RGBV) model in the materials science community [65,66]. It should be noted that both of these models contain several additional parameters that require fitting and experimental validations and may lead to more uncertainties.

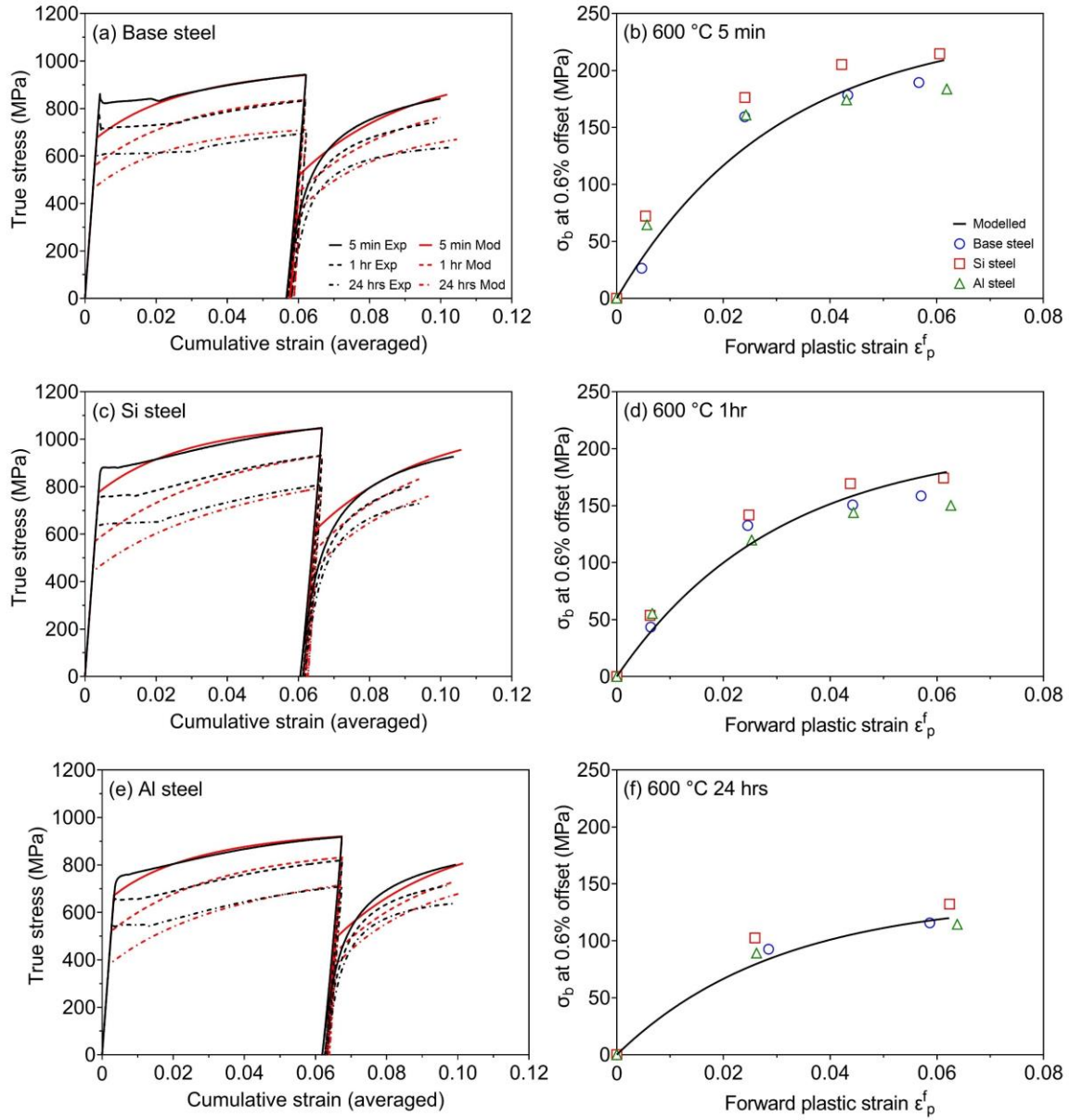


Figure 11 (a), (c) and (e) Experimental and modelled tension-compression curves for the 600 °C tempered samples. (b), (d) and (f) Evolution of the back stress at 0.6% offset and the modelled back stress as a function of forward plastic strain for the 600 °C tempered samples.

Table 3 summarises the values of optimised parameters (V_f^g and k_2) used in the model. These two parameters are the ones that most affect the modelled results. To best describe the experimental results, the volume fraction of the precipitates within grains for all steels is set to be 0.035, 0.03 and 0.02 for the 5-minute, 1-hour, 24-hour tempered conditions respectively. This estimate qualitatively agrees with the SEM investigation (Figure 10) where the precipitates within the laths are becoming fewer in number or fraction as tempering proceeds. One way to quantitatively assess the validity of the estimate is to compare the modelled and experimentally measured back stress (Figure 11b, d and f). Both the evolution and the magnitude of the offset back stress can be well reproduced by the kinematic hardening model using the estimated volume fractions for all tempering times.

Table 3 V_f^g and k_2 values used in the modelled curves.

Parameter	Steel grade	600 °C 5 min	600 °C 1 hr	600 °C 24 hrs
V_f^g	All steels	0.035	0.03	0.02
	Base steel	57	35	35
k_2	Si steel	56	12	9
	Al steel	94	25	12

Another way to test the reasonableness of values used is to use metallography to estimate the volume fraction of precipitates on grain boundaries V_f^{gb} and back calculate the value of V_f^g . This method reduces some uncertainties in highlighting small precipitates within grains. Figure 12a shows an SEM image in the Base steel sample tempered at 600 °C for 24 hours etched with Nital which highlights both ferrite grain boundaries and cementite particles. Particles on the grain boundaries can be highlighted and analysed to estimate the average particles size r_g and the areal number density N_s^{gb} (Figure 12b). The volumetric number density and volume fraction can be estimated as $N_v^{gb} = 2r_{gb}$ and $V_f^{gb} = N_v^{gb} \cdot \frac{4}{3}\pi r_{gb}^3$ [67]. Several field views in samples tempered at 600 °C for 24 hours were analysed and the estimated volume fraction at grain boundaries is ~ 0.022 , which results in a V_f^g of 0.0155. Considering the uncertainties in estimating volume fraction using 2-D images, this estimate is in good agreement with the value used in the model.

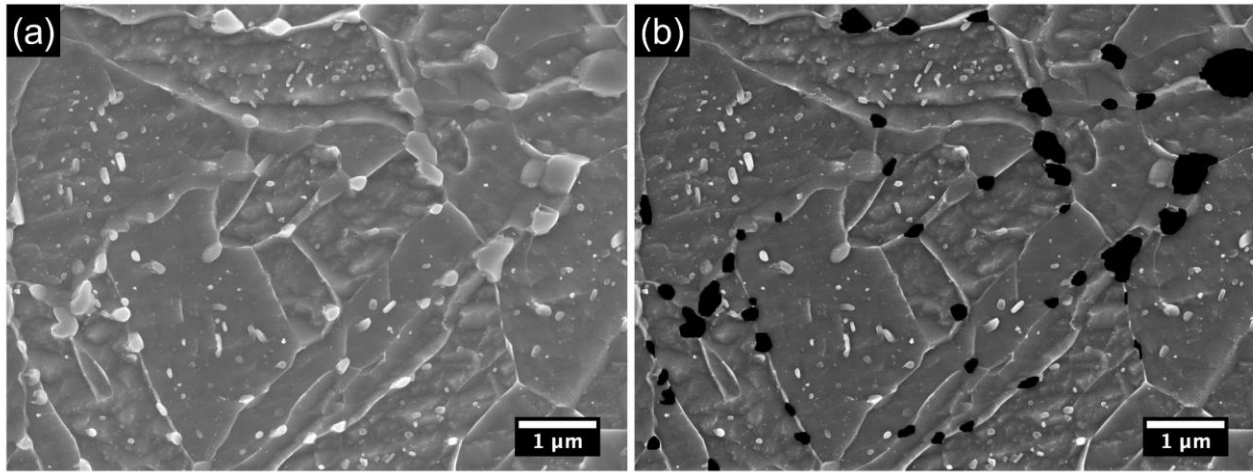


Figure 12 Estimation of volume fraction precipitates on grain boundaries. (a) Original SEM image from a Base steel sample tempered at 600 °C for 24 hours. (b) Particles on grain boundaries highlighted for image analysis in ImageJ. Etched with Nital.

Finally, we come to the single parameter that needs to be optimised for each tempering condition, k_2 (Table 3). It can be seen that the values start very high in the 5-minute tempered states and decrease as a function of tempering time. Typical values of k_2 in coarse grain ferritic steels are around 7 - 22 [68], which correspond well with the values in 1-hour and 24-hours tempered samples. The high values in 5-minute tempered samples can be again attributed to the small spacing between grain boundaries which increases the probability of dislocation annihilation at grain boundaries [56,57].

4.1.5 Limitation of the combined hardening model for samples with low strain hardening response

Since this combined hardening model works well for the 600 °C tempered conditions, we have attempted to implement the same model for the samples tempered at 500 °C and 400 °C. However, the model is not able to describe fully the tension-compression behaviour of the material. Figure 13a shows the comparison between the experimental and modelled curves for samples tempered at 500 °C for 5 minutes considering only the kinematic hardening contribution from the cementite precipitates ($V_f = 0.0375$, $k_1 = 0$). Although the forward loading can be reproduced, the modelled curve significantly underestimates the Bauschinger effect in the reverse loading direction. This discrepancy can be attributed to an underestimated back stress as shown in Figure 13b and suggests that the kinematic hardening contribution from precipitates alone cannot reproduce the reduction in reverse yield strength and additional kinematic hardening contributions need to be included. The underestimated kinematic hardening could be achieved by incorporating the contribution from grain boundaries as suggested in the work of Kim et al. [24]. However, if the kinematic hardening contributions from both precipitates and grain boundaries are considered, the model will greatly overestimate the hardening in the forward direction since the measurable strain hardening is only ~150 MPa, which is much smaller than the measured kinematic hardening ~250 MPa. The low strain hardening and large Bauschinger effect observed in the 500 °C and 400 °C tempered samples are the major obstacles for the future improvement of the model. These conditions, at the boundary between the low temperature tempering and high temperature tempering regimes, are well worth further dedicated study.

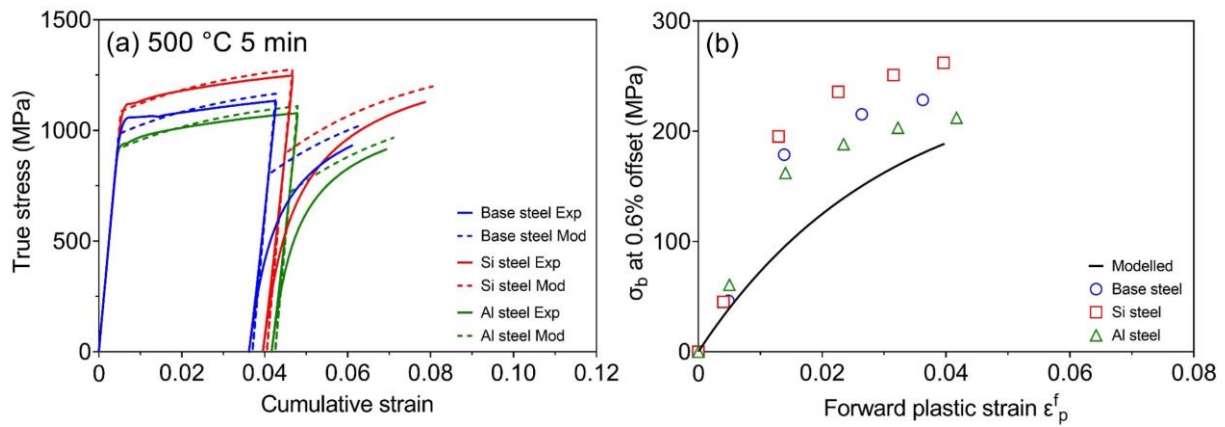


Figure 13 (a) Experimental and modelled tension-compression curve for the Si steel tempered at 500 °C for 5 minutes. (b) The evolution of the back stress at 0.6% offset and the modelled back stress as a function of forward plastic strain for the samples tempered at 500 °C for 5 minutes. The experimental data points in (b) were obtained from the re-analyses of data published in [37].

4.2 Perspectives on the strain hardening of tempered martensite at intermediate temperatures

4.2.1 Effect of Si and Al additions on the transition in the flow behaviour of tempered martensite

Si and Al are primarily added to AHSS's to modify the cementite precipitation kinetics and the chemistry within the cementite. While these effects are still present at higher tempering temperatures, their influence on the strain hardening and softening of martensite is most significant at lower temperatures (Figure 5d). The most noticeable impact of the alloying elements on martensite softening is found in the evolution of the microstrain during low temperature tempering and straining: (1) the elements significantly retard the overall reduction of the microstrain during tempering (Figure 3b); (2) samples with alloying elements show much larger reduction in microstrain during straining after tempered at 300 °C and 400 °C (Figure 6 and [8]). If the diffraction line breadth of as-quenched and low temperature tempered martensite is caused by the combined effect of dislocations and transformation induced residual stresses, it is reasonable to deduce that the main contribution of Si and Al is to slow down the thermal relaxation of the transformation induced residual stresses and not necessarily the retardation of dislocation recovery [69,70]. The reduced softening kinetics should then be attributed to the remaining “composite” heterogeneity in the alloyed samples.

4.2.2 The origin of the low strain hardening response in intermediate temperature tempered martensite

In previous [8] and current investigations, two models that describe the strain hardening behaviour of martensite under two “extreme” conditions have been proposed: the as-quenched and low temperature tempered conditions, and the high temperature tempered condition. These two tempering conditions, combined with their relatively high strain hardening exponents, occupy the top left and top right corners of Figure 5c. While the two models can be extended to conditions with lower strain hardening exponents, both models have difficulties in rationalising the tension-compression flow behaviour of martensite tempered at intermediate temperatures (i.e. 400 °C and 500 °C). The key characteristics of this transition observed at intermediate temperature tempering conditions are: (1) the strain hardening rate after the macroscopic yield point drops to around or below the E/50 limit; (2) the diffraction peak narrowing phenomenon transitions into to limited narrowing or peak broadening during forward straining; (3) samples show a minimum strain hardening exponent and the tensile curves in the forward direction are relatively flat; (4) despite the low strain hardening in the forward direction, the Bauschinger effect is still large during strain reversal, indicating a large kinematic hardening contribution.

In appearance, similar transitional features were reported by Ohmura and co-workers in the nanohardness response of tempered Fe-C martensite [71–73]. They observed that the ratio between the nanohardness and microhardness (H_n/H_v) witnessed a sharp increase around 400 °C and attributed this increase to the reduction in the grain refinement effect from martensite laths/blocks. It was rationalised by TEM observations where thin-film carbides transformed into spheroidised carbides above this transition temperature, which reduced the k factor in the Hall-Petch equation. Evidence for the reduced k factor can be found in early works from Swarr and Krauss where the authors demonstrated that the k factor in 400 °C tempered martensite was much lower than the one measured in as-quenched martensite [11]. While the above experimental findings are true, this

theory cannot explain the significantly reduced strain hardening in intermediate temperature tempered martensite.

Based on the deformation and microstructural characteristics discussed above, it is suggested that the low strain hardening response of intermediate temperature tempered martensite is likely due to the combined effect of the ultra-fine grained nature of martensitic structures and the lost composite effect from tempering. Figure 14 shows the arithmetic average grain size of the studied steels as a function of tempering and highlights that the grain size is around 0.8 μm until 600 $^{\circ}\text{C}$. It is appropriate to consider martensite an ultra-fine grained material. Ultra-fine grained ferrite/ferrite-cementite steels lack strain hardening due to the dislocation sinks at grain boundaries especially when the grain size is below 1 μm [44,52,74]. When the composite effect from transformation induced residual stresses and/or the yield strength spectrum is present, it provides the large strain hardening rate observed in the Kocks-Mecking plots (Figure 4b, d, f). When the composite effect is partially relaxed by tempering, the strain hardening rate is reduced, which leads to low strain hardening rates observed in ultra-fine grained ferrite. As the dislocation density further decreases and the martensite blocks start to grow at higher temperatures, the dislocations are able to accumulate and deposit Orowan loops on cementite precipitates which promotes strain hardening in martensite. A critical question becomes how to simultaneously address the low strain hardening and large Bauschinger effect observed in intermediate temperature tempered samples. This is a major unanswered question that must be addressed.

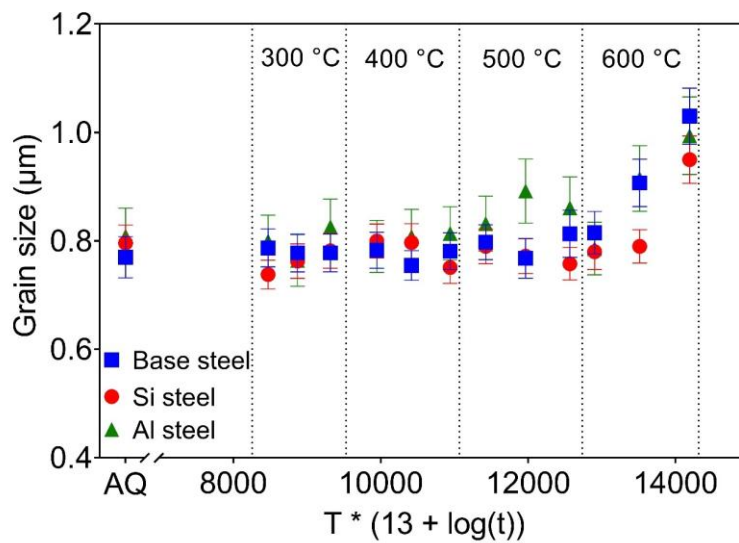


Figure 14 Hollomon-Jaffe plot showing the evolution of the effective grain size (equivalent grain diameter) as a function of tempering parameters. At each temperature, three tempering times were shown (i.e. 1 minute, 5 minutes and 30 minutes). Error bars represent the 95% confidence interval of the calculated averages.

4.2.3 Towards a unified plasticity model for martensite

In light of the above discussions, intermediate temperature tempered martensites possess characteristics from both composite and dislocation-based models and a unified plasticity model is required to self-consistently

explain the flow behaviour of intermediate temperature tempered martensite. The unified plasticity model should include the following ingredients:

- A convoluted yield stress and residual stress spectrum model addressing the mechanical heterogeneities induced during the martensitic transformation. This is captured in the recent “integral composite model” [8] but the detailed convolution function remains unclear.
- An isotropic hardening model focusing on the thermal, dislocation-based strengthening. This term was omitted in the “integral composite model” for as-quenched and low temperature tempered martensite but it will become increasingly important as tempering proceeds [37].
- A kinematic hardening model addressing the athermal, long-range strengthening components that result in the Bauschinger effect. A model combining the effect of mesoscopic mechanical incompatibility (composite effects) and the contribution of microscopic features is required.
- A grain size dependent hardening component highlighting the effect of ultra-fine grains on the low strain hardening response.

Although most of the problems listed above have now been addressed, the composite strengthening model and the isotropic-kinematic hardening model are implemented separately and the combination remains a challenging task. In addition, the unified plasticity model also needs to be coupled with several tempering events:

- The relaxation kinetics of transformation induced residual stresses and dislocation densities need to be decoupled and described quantitatively. It will further understanding of the carriers of these peak-broadening terms and their evolution kinetics.
- The precipitation kinetics of transition carbides and cementite at intermediate temperatures need to be quantified. Although substantial experimental works have been performed in characterising these carbides and their evolutions [75–77], a dedicated kinetics model like the one developed by Wu et al. [33,34] for high temperatures is required.
- As a result of relaxation of microstrains and carbide precipitation, there should be a decrease in the intrinsic width of the yield stress spectrum as predicted by Cupertino Malheiros et al. [23], which could partially explain the reduced Bauschinger effect. It would be interesting if the softening kinetics of the localised yield strength can be linked to the softening kinetics of bulk martensite.

It is worth noting that these tempering events are strongly correlated and need dedicated experimental campaigns to decouple. For example, it is shown that the addition of Si and Al is able to affect all three tempering events listed above, which brings further complexities. The aforementioned mechanical and microstructural components are essential to develop a unified and physically-sound constitutive model for not only intermediate temperature tempered martensite, but for ferrous martensite in general.

5 Conclusion

A systematic study on the deformation mechanisms of tempered martensitic steels has been conducted. At lower tempering temperatures (300 °C and 400 °C), the strain hardening response of tempered martensite resembles the as-quenched state (i.e. greater than the E/50 limit). However, a continuous loss of strain hardening capacity is observed during tempering, which can be attributed to the progressive elimination of the composite strengthening contributions. The addition of Si and Al has a significant impact on the softening kinetics at this stage and their contribution is two-fold: (1) Si and Al retard the precipitation of cementite, which could allow more carbon to segregate on dislocations and reduces the kinetics of dislocation recovery; (2) the transformation induced residual stress relaxes slower in the Si and Al added steels, which allows the steels to retain much of the composite strengthening, leading to larger strain hardening exponents and slower softening kinetics compared to the Base steel. The physical mechanisms that drive the relaxation of residual stresses requires further studies.

At higher tempering temperatures (500 °C and 600 °C), the strain hardening rates of all samples are below the E/50 limit, interrupted X-ray diffraction experiments show diffraction peak broadening, and the strain hardening capacity increases. The effect of Si and Al are significantly reduced at high temperatures due to the enhanced precipitation kinetics. The results indicate that it is possible to model the flow behaviour of high temperature tempered martensite using dislocation-based models. In this case, the modelling framework is proposed so that no mechanical “composite” heterogeneity exists in the microstructure and the constituents are allowed to harden through a combination of isotropic hardening and kinematic hardening mechanisms. Using modelling parameters obtained from the literature and microscopy works performed in this study, the combined hardening model is capable of describing the tension-compression flow behaviour of 600 °C tempered samples, but not at 500 °C. Further investigations are needed to simultaneously address the low strain hardening in the forward direction and the large Bauschinger effect during strain reversal. It is suggested that the key to solve this problem is to combine the composite and isotropic-kinematic hardening models together with dedicated experiments to monitor the microstructural changes influencing the parameters used in the model.

Acknowledgments

The authors would like to thank the support of ArcelorMittal and the Australian Research Council through the Linkage Grant Scheme (LP150100756). LYW would like to acknowledge the support of the Fundamental Research Funds for the Central Universities (N2107005), the National Natural Science Foundation of China (Grant No. U1808208, Grant No. 51961130389) and Prof. Wei Xu for fruitful discussions. YXW and LYW gratefully acknowledge the award of the Australian Government Research Training Program. Mr. Xiang Gao is acknowledged for preparing the TEM samples and acquiring some of the TEM images. Dr. Qi Zhang is acknowledged for helping with the DSC tests. The authors would also like to express thanks for the use of equipment within the Monash Centre for Electron Microscopy (MCEM) and the Monash X-Ray Platform (MXP).

References

- [1] G. Krauss, *Steels: processing, structure, and performance*, ASM International, 2015.
- [2] S. Allain, O. Bouaziz, M. Takahashi, Toward a New Interpretation of the Mechanical Behaviour of As-quenched Low Alloyed Martensitic Steels, *ISIJ Int.* 52 (2012) 717–722. doi:10.2355/isijinternational.52.717.
- [3] C.P. Scott, B. Shalchi Amirkhiz, I. Pushkareva, F. Fazeli, S.Y.P. Allain, H. Azizi, New insights into martensite strength and the damage behaviour of dual phase steels, *Acta Mater.* 159 (2018) 112–122. doi:10.1016/j.actamat.2018.08.010.
- [4] M. Juan, G. Steve, G. Guillaume, T. Julien, D. Sabine, B. Frédéric, A.S.Y. P., Dislocation densities in a low-carbon steel during martensite transformation determined by in situ high energy X-Ray diffraction, *Mater. Sci. Eng. A.* 800 (2020) 140249. doi:10.1016/j.msea.2020.140249.
- [5] B. Hutchinson, D. Lindell, M. Barnett, Yielding Behaviour of Martensite in Steel, *ISIJ Int.* 55 (2015) 1114–1122. doi:10.2355/isijinternational.55.1114.
- [6] B. Hutchinson, P. Bate, D. Lindell, A. Malik, M. Barnett, P. Lynch, Plastic yielding in lath martensites - An alternative viewpoint, *Acta Mater.* 152 (2018) 239–247. doi:10.1016/j.actamat.2018.04.039.
- [7] B. Hutchinson, J. Brask, An Investigation of Short Range Residual Stress Fields in Ferrous Lath Martensite, *Metall. Mater. Trans. A.* 50 (2019) 5581–5584. doi:10.1007/s11661-019-05501-9.
- [8] L.Y. Wang, Y.X. Wu, W.W. Sun, Y. Bréchet, L. Brassart, A. Arlazarov, C.R. Hutchinson, Strain hardening behaviour of as-quenched and tempered martensite, *Acta Mater.* 199 (2020) 613–632. doi:10.1016/j.actamat.2020.08.067.
- [9] G.R. Speich, Tempering of Low-Carbon Martensite, *Trans. Metall. Soc. AIME.* 245 (1969) 2553–2564.
- [10] G.R. Speich, W.C. Leslie, Tempering of steel, *Metall. Trans.* 3 (1972) 1043–1054. doi:10.1007/BF02642436.
- [11] T. Swarr, G. Krauss, The effect of structure on the deformation of as-quenched and tempered martensite in an Fe-0.2 pct C alloy, *Metall. Trans. A.* 7 (1976) 41–48. doi:10.1007/BF02644037.
- [12] M.A. Zacccone, G. Krauss, Elastic limits and microplastic response in ultrahigh strength carbon steels, *Metall. Trans. A.* 20 (1989) 188–191. doi:10.1007/BF02647507.
- [13] G. Krauss, Heat Treated Martensitic Steels: Microstructural Systems for Advanced Manufacture., *ISIJ Int.* 35 (1995) 349–359. doi:10.2355/isijinternational.35.349.
- [14] R.N. Caron, G. Krauss, The tempering of Fe-C lath martensite, *Metall. Trans.* 3 (1972) 2381–2389. doi:10.1007/BF02647041.
- [15] M.A. Zacccone, G. Krauss, Elastic limit and microplastic response of hardened steels, *Metall. Trans. A.* 24 (1993) 2263–2277. doi:10.1007/BF02648600.
- [16] M. Saeglitz, G. Krauss, Deformation, fracture, and mechanical properties of low-temperature-tempered martensite in SAE 43xx steels, *Metall. Mater. Trans. A.* 28 (1997) 377–387. doi:10.1007/s11661-997-0139-x.
- [17] G. Krauss, Martensite in steel: strength and structure, *Mater. Sci. Eng. A.* 273–275 (1999) 40–57. doi:10.1016/S0921-5093(99)00288-9.

- [18] G. Krauss, Deformation and fracture in martensitic carbon steels tempered at low temperatures, *Metall. Mater. Trans. B.* 32 (2001) 205–221. doi:10.1007/s11663-001-0044-4.
- [19] G. Krauss, Tempering of Lath Martensite in Low and Medium Carbon Steels: Assessment and Challenges, *Steel Res. Int.* 87 (2017) 1700038. doi:10.1002/srin.201700038.
- [20] U.F. Kocks, H. Mecking, Physics and phenomenology of strain hardening: The FCC case, *Prog. Mater. Sci.* 48 (2003) 171–273. doi:10.1016/S0079-6425(02)00003-8.
- [21] E.I. Galindo-Nava, P.E.J. Rivera-Díaz-del-Castillo, A model for the microstructure behaviour and strength evolution in lath martensite, *Acta Mater.* 98 (2015) 81–93. doi:10.1016/j.actamat.2015.07.018.
- [22] L. Malik, J.A. Lund, A study of strengthening mechanisms in tempered martensite from a medium carbon steel, *Metall. Trans.* 3 (1972) 1403–1406. doi:10.1007/BF02643024.
- [23] L.R. Cupertino Malheiros, E.A. Pachon Rodriguez, A. Arlazarov, Mechanical behavior of tempered martensite: Characterization and modeling, *Mater. Sci. Eng. A.* 706 (2017) 38–47. doi:10.1016/j.msea.2017.08.089.
- [24] B. Kim, E. Boucard, T. Sourmail, D. San Martín, N. Gey, P.E.J. Rivera-Díaz-del-Castillo, The influence of silicon in tempered martensite: Understanding the microstructure–properties relationship in 0.5–0.6wt.% C steels, *Acta Mater.* 68 (2014) 169–178. doi:10.1016/j.actamat.2014.01.039.
- [25] L.M. Brown, W.M. Stobbs, The work-hardening of copper-silica I. A model based on internal stresses with no plastic relaxation, *Philos. Mag.* 23 (1971) 1185–1199. doi:10.1080/14786437108217405.
- [26] L.M. Brown, W.M. Stobbs, The work-hardening of copper-silica II. The role of plastic relaxation, *Philos. Mag.* 23 (1971) 1201–1233. doi:10.1080/14786437108217406.
- [27] J.D. Atkinson, L.M. Brown, W.M. Stobbs, The work-hardening of copper-silica: IV. The Bauschinger effect and plastic relaxation, *Philos. Mag.* 30 (1974) 1247–1280. doi:10.1080/14786437408207280.
- [28] L.M. Brown, D.R. Clarke, Work hardening due to internal stresses in composite materials, *Acta Metall.* 23 (1975) 821–830. doi:10.1016/0001-6160(75)90198-4.
- [29] Y.W. Chang, R.J. Asaro, Bauschinger effects and work-hardening in spheroidized steels, *Met. Sci.* 12 (1978) 277–284. doi:10.1179/030634578790433756.
- [30] R.A. Barrett, P.E. O'Donoghue, S.B. Leen, A physically-based constitutive model for high temperature microstructural degradation under cyclic deformation, *Int. J. Fatigue.* 100 (2017) 388–406. doi:10.1016/j.ijfatigue.2017.03.018.
- [31] D.F. Li, R.A. Barrett, P.E. O'Donoghue, N.P. O'Dowd, S.B. Leen, A multi-scale crystal plasticity model for cyclic plasticity and low-cycle fatigue in a precipitate-strengthened steel at elevated temperature, *J. Mech. Phys. Solids.* 101 (2017) 44–62. doi:10.1016/j.jmps.2016.12.010.
- [32] G. Miyamoto, J.C. Oh, K. Hono, T. Furuhashi, T. Maki, Effect of partitioning of Mn and Si on the growth kinetics of cementite in tempered Fe-0.6 mass% C martensite, *Acta Mater.* 55 (2007) 5027–5038. doi:10.1016/j.actamat.2007.05.023.
- [33] Y.X. Wu, W.W. Sun, M.J. Styles, A. Arlazarov, C.R. Hutchinson, Cementite coarsening during the tempering of Fe-C-Mn martensite, *Acta Mater.* 159 (2018) 209–224. doi:10.1016/j.actamat.2018.08.023.

- [34] Y.X. Wu, W.W. Sun, X. Gao, M.J. Styles, A. Arlazarov, C.R. Hutchinson, The effect of alloying elements on cementite coarsening during martensite tempering, *Acta Mater.* 183 (2020) 418–437. doi:10.1016/j.actamat.2019.11.040.
- [35] K.Y. Zhu, H. Shi, H. Chen, C. Jung, Effect of Al on martensite tempering: comparison with Si, *J. Mater. Sci.* 53 (2018) 6951–6967. doi:10.1007/s10853-018-2037-6.
- [36] Y.X. Wu, *Phase Transformations during the Processing of Third Generation Advanced High Strength Steels*, Monash University, 2019.
- [37] L.Y. Wang, Y.X. Wu, W.W. Sun, Y. Bréchet, L. Brassart, A. Arlazarov, C.R. Hutchinson, Thermal and athermal contributions to the flow stress of martensite, *Materialia*. 11 (2020) 100719. doi:10.1016/j.mtla.2020.100719.
- [38] D. Balzar, Voigt-function model in diffraction line-broadening analysis, in: R.L. Snyder, H.J. Bunge, J. Fiala (Eds.), *Microstruct. Anal. from Diffr.*, International Union of Crystallography, 1999. doi:10.1.1.30.7311.
- [39] T. Ungár, S. Harjo, T. Kawasaki, Y. Tomota, G. Ribárik, Z.M. Shi, Composite Behavior of Lath Martensite Steels Induced by Plastic Strain, a New Paradigm for the Elastic-Plastic Response of Martensitic Steels, *Metall. Mater. Trans. A.* 48 (2017) 159–167. doi:10.1007/s11661-016-3845-4.
- [40] S. Harjo, T. Kawasaki, Y. Tomota, W. Gong, K. Aizawa, G. Tichy, Z.G. Shi, T. Ungár, Work Hardening, Dislocation Structure, and Load Partitioning in Lath Martensite Determined by In Situ Neutron Diffraction Line Profile Analysis, *Metall. Mater. Trans. A.* 48 (2017) 4080–4092. doi:10.1007/s11661-017-4172-0.
- [41] É. Ódor, B. Jóni, G. Ribárik, N.Q. Chinh, T. Ungár, P.J. Szabó, Deformation Induced Soft and Hard Lath Packets Enhance Ductility in Martensitic Steels, *Crystals*. 10 (2020) 373. doi:10.3390/cryst10050373.
- [42] E. De Moor, S. Lacroix, L. Samek, J. Penning, J.G. Speer, Dilatometric study of the quench and partitioning process, in: *3rd Int. Conf. Adv. Struct. Steels*, Gyeongju, Korea, 2006: pp. 873–878. doi:http://dx.doi.org/10.1016/j.ijplas.2008.03.009.
- [43] J.H. Hollomon, Tensile Deformation, *Trans. Metall. Soc. AIME*. 162 (1945) 268–290.
- [44] N. Tsuchida, H. Masuda, Y. Harada, K. Fukaura, Y. Tomota, K. Nagai, Effect of ferrite grain size on tensile deformation behavior of a ferrite-cementite low carbon steel, *Mater. Sci. Eng. A.* 488 (2008) 446–452. doi:10.1016/j.msea.2007.11.047.
- [45] V.K. Judge, *Effects of Short-Time Tempering on Mechanical Properties and Fracture of 4340 Steel*, Colorado School of Mines, 2017.
- [46] J.L. Chaboche, A review of some plasticity and viscoplasticity constitutive theories, *Int. J. Plast.* 24 (2008) 1642–1693. doi:10.1016/j.ijplas.2008.03.009.
- [47] C. Laird, H.I. Aaronson, Structures and Migration Kinetics of Alpha:Theta Prime Boundaries in Al-4 Pct Cu: Part I - Interfacial Structures, *Trans. Metall. Soc. AIME*. 242 (1968) 1393. doi:10.1017/CBO9781107415324.004.
- [48] C. Calabrese, C. Laird, Cyclic stress-strain response of two-phase alloys Part I. Microstructures

containing particles penetrable by dislocations, *Mater. Sci. Eng.* 13 (1974) 141–157. doi:10.1016/0025-5416(74)90182-7.

- [49] J. da Costa Teixeira, L. Bourgeois, C.W. Sinclair, C.R. Hutchinson, The effect of shear-resistant, plate-shaped precipitates on the work hardening of Al alloys: Towards a prediction of the strength-elongation correlation, *Acta Mater.* 57 (2009) 6075–6089. doi:10.1016/j.actamat.2009.08.034.
- [50] C.W. Sinclair, W.J. Poole, Y. Bréchet, A model for the grain size dependent work hardening of copper, *Scr. Mater.* 55 (2006) 739–742. doi:10.1016/j.scriptamat.2006.05.018.
- [51] S. Cobo, O. Bouaziz, Investigations and Modelling of the Work Hardening of As-Quenched Martensite, in: *New Dev. Metall. Appl. High Strength Steels*, Buenos Aires 2008 - Proc. Int. Conf. New Dev. Metall. Appl. High Strength Steels, 2008: pp. 909–918.
- [52] H. Li, S. Gao, Y. Tomota, S. Ii, N. Tsuji, T. Ohmura, Mechanical response of dislocation interaction with grain boundary in ultrafine-grained interstitial-free steel, *Acta Mater.* 206 (2021) 116621. doi:10.1016/j.actamat.2021.116621.
- [53] H. Proudhon, W.J. Poole, X. Wang, Y. Bréchet, The role of internal stresses on the plastic deformation of the Al-Mg-Si-Cu alloy AA6111, *Philos. Mag.* 88 (2008) 621–640. doi:10.1080/14786430801894569.
- [54] C. Jiang, S.G. Srinivasan, A. Caro, S.A. Maloy, Structural, elastic, and electronic properties of Fe₃C from first principles, *J. Appl. Phys.* 103 (2008). doi:10.1063/1.2884529.
- [55] F. Laszlo, H. Nolle, On some physical properties of cementite, *J. Mech. Phys. Solids.* 7 (1959). doi:10.1016/0022-5096(59)90006-7.
- [56] G.A. Malygin, Strength and plasticity of nanocrystalline materials and nanosized crystals, *Physics-Uspekhi.* 54 (2011) 1091–1116. doi:10.3367/ufne.0181.201111a.1129.
- [57] S.H. He, K.Y. Zhu, M.X. Huang, A unified dislocation-based model for ultrafine- and fine-grained face-centered cubic and body-centered cubic metals, *Comput. Mater. Sci.* 131 (2017) 1–10. doi:10.1016/j.commatsci.2017.01.022.
- [58] D. Bardel, M. Perez, D. Nelias, S. Dancette, P. Chaudet, V. Massardier, Cyclic behaviour of a 6061 aluminium alloy: Coupling precipitation and elastoplastic modelling, *Acta Mater.* 83 (2014) 256–268. doi:10.1016/j.actamat.2014.09.034.
- [59] R. Schwab, V. Ruff, On the nature of the yield point phenomenon, *Acta Mater.* 61 (2013) 1798–1808. doi:10.1016/j.actamat.2012.12.003.
- [60] J.P.G. Sawyer, C.H. Wang, R. Jones, An implicit algorithm using explicit correctors for the kinematic hardening model with multiple back stresses, *Int. J. Numer. Methods Eng.* 50 (2001) 2093–2107.
- [61] U.F. Kocks, The relation between polycrystal deformation and single-crystal deformation, *Metall. Mater. Trans.* 1 (1970) 1121–1143. doi:10.1007/BF02900224.
- [62] E.J. Seo, L. Cho, Y. Estrin, B.C. De Cooman, Microstructure-mechanical properties relationships for quenching and partitioning (Q&P) processed steel, *Acta Mater.* 113 (2016) 124–139. doi:10.1016/j.actamat.2016.04.048.
- [63] F. Yoshida, T. Uemori, A model of large-strain cyclic plasticity describing the Bauschinger effect and workhardening stagnation, *Int. J. Plast.* 18 (2002) 661–686. doi:10.1016/S0749-6419(01)00050-X.

- [64] F. Yoshida, T. Uemori, K. Fujiwara, Elastic-plastic behavior of steel sheets under in-plane cyclic tension-compression at large strain, *Int. J. Plast.* 18 (2002) 633–659. doi:10.1016/S0749-6419(01)00049-3.
- [65] E.F. Rauch, J.J. Gracio, F. Barlat, Work-hardening model for polycrystalline metals under strain reversal at large strains, *Acta Mater.* 55 (2007) 2939–2948. doi:10.1016/j.actamat.2007.01.003.
- [66] E.F. Rauch, J.J. Gracio, F. Barlat, G. Vincze, Modelling the plastic behaviour of metals under complex loading conditions, *Model. Simul. Mater. Sci. Eng.* 19 (2011). doi:10.1088/0965-0393/19/3/035009.
- [67] R.L. Fullman, Measurement of Particle Sizes in Opaque Bodies, *JOM.* 5 (1953) 447–452. doi:10.1007/bf03398971.
- [68] X.F. Fang, W. Dahl, Strain hardening of steels at large strain deformation. Part I: Relationship between strain hardening and microstructures of b.c.c. steels, *Mater. Sci. Eng. A.* 203 (1995) 14–25. doi:10.1016/0921-5093(95)09841-0.
- [69] B. Kim, D. San-Martin, P.E.J. Rivera-Díaz-del-Castillo, Modelling recovery kinetics in high-strength martensitic steels, *Philos. Mag. Lett.* 97 (2017) 280–286. doi:10.1080/09500839.2017.1342048.
- [70] J. Klemm-Toole, J. Benz, I. Vieira, A.J. Clarke, S.W. Thompson, K.O. Findley, Strengthening mechanisms influenced by silicon content in high temperature tempered martensite and bainite, *Mater. Sci. Eng. A.* 786 (2020) 139419. doi:10.1016/j.msea.2020.139419.
- [71] T. Ohmura, K. Tsuzaki, S. Matsuoka, Evaluation of the matrix strength of Fe-0.4 wt% C tempered martensite using nanoindentation techniques, *Philos. Mag. A Phys. Condens. Matter, Struct. Defects Mech. Prop.* 82 (2002) 1903–1910. doi:10.1080/01418610208235702.
- [72] T. Ohmura, T. Hara, K. Tsuzaki, Relationship between nanohardness and microstructures in high-purity Fe-C as-quenched and quench-tempered martensite, *J. Mater. Res.* 18 (2003) 1465–1470. doi:10.1557/JMR.2003.0201.
- [73] T. Ohmura, T. Hara, K. Tsuzaki, Evaluation of temper softening behavior of Fe-C binary martensitic steels by nanoindentation, *Scr. Mater.* 49 (2003) 1157–1162. doi:10.1016/j.scriptamat.2003.08.025.
- [74] R. Song, D. Ponge, D. Raabe, Mechanical properties of an ultrafine grained C-Mn steel processed by warm deformation and annealing, *Acta Mater.* 53 (2005) 4881–4892. doi:10.1016/j.actamat.2005.07.009.
- [75] D.T. Pierce, D.R. Coughlin, D.L. Williamson, K.D. Clarke, A.J. Clarke, J.G. Speer, E. De Moor, Characterization of transition carbides in quench and partitioned steel microstructures by Mössbauer spectroscopy and complementary techniques, *Acta Mater.* 90 (2015) 417–430. doi:10.1016/j.actamat.2015.01.024.
- [76] D.T. Pierce, D.R. Coughlin, D.L. Williamson, J. Kähkönen, A.J. Clarke, K.D. Clarke, J.G. Speer, E. De Moor, Quantitative investigation into the influence of temperature on carbide and austenite evolution during partitioning of a quenched and partitioned steel, *Scr. Mater.* 121 (2016) 5–9. doi:10.1016/j.scriptamat.2016.04.027.
- [77] A.J. Clarke, J. Klemm-Toole, K.D. Clarke, D.R. Coughlin, D.T. Pierce, V.K. Euser, J.D. Poplawsky, B. Clausen, D. Brown, J. Almer, P.J. Gibbs, D.J. Alexander, R.D. Field, D.L. Williamson, J.G. Speer,

G. Krauss, Perspectives on Quenching and Tempering 4340 Steel, *Metall. Mater. Trans. A.* 51 (2020) 4984–5005. doi:10.1007/s11661-020-05972-1.